The Astrophysical Journal, 778:47 (21pp), 2013 November 20 doi:10.1088/0004-637X/778/1/47

REFINING THE M_{BH}–V_c SCALING RELATION WITH H I ROTATION CURVES OF WATER MEGAMASER GALAXIES

Ai-Lei Sun[1], Jenny E. Greene[1,5], C. M. Violette Impellizzeri[2,6], Cheng-Yu Kuo[3], James A. Braatz[2], and Sarah Tuttle[4]
[1] Department of Astrophysics, Princeton University, Princeton, NJ 08540, USA
[2] National Radio Astronomy Observatory, 520 Edgemont Road, Charlottesville, VA 22903, USA
[3] Academia Sinica Institute of Astronomy and Astrophysics, P.O. Box 23-141, Taipei 10617, Taiwan
[4] McDonald Observatory, The University of Texas, Austin, TX 78712, USA
Received 2013 June 5; accepted 2013 September 12; published 2013 November 1

ABSTRACT

Black-hole–galaxy scaling relations provide information about the coevolution of supermassive black holes and their host galaxies. We compare the black-hole mass–circular-velocity (M_{BH}–V_c) relation with the black-hole-mass–bulge-stellar-velocity-dispersion (M_{BH}–σ_*) relation to see whether the scaling relations can passively emerge from a large number of mergers or require a physical mechanism, such as feedback from an active nucleus. We present Very Large Array H I observations of five galaxies, including three water megamaser galaxies, to measure the circular velocity. Using 22 galaxies with dynamical M_{BH} measurements and V_c measurements extending to large radius, our best-fit M_{BH}–V_c relation, $\log M_{BH} = \alpha + \beta \log(V_c/200\ \mathrm{km\ s^{-1}})$, yields $\alpha = 7.43^{+0.13}_{-0.13}$, $\beta = 3.68^{+1.23}_{-1.20}$, and an intrinsic scatter $\epsilon_{int} = 0.51^{+0.11}_{-0.09}$. The intrinsic scatter may well be higher than 0.51, as we take great care to ascribe conservatively large observational errors. We find comparable scatter in the M_{BH}–σ_* relations, $\epsilon_{int} = 0.48^{+0.10}_{-0.08}$, while pure merging scenarios would likely result in a tighter scaling with the dark halo (as traced by V_c) properties rather than the baryonic (σ_*) properties. Instead, feedback from the active nucleus may act on bulge scales to tighten the M_{BH}–σ_* relation with respect to the M_{BH}–V_c relation, as observed.

Key word: quasars: supermassive black holes

Online-only material: color figures

1. INTRODUCTION

The observed scaling relations between supermassive black hole (BH) mass and properties of the host galaxy, intensively studied over the past decade, suggest that BH growth is tied to the growth of the surrounding host galaxy. These galaxy properties include the bulge/spheroid stellar velocity dispersion σ_* (e.g., Ferrarese & Merritt 2000; Tremaine et al. 2002; Gültekin et al. 2009; Beifiori et al. 2012; McConnell & Ma 2013), the mass and luminosity of galaxy bulges (e.g., Marconi & Hunt 2003; Häring & Rix 2004; McConnell & Ma 2013), and the circular velocity V_c (e.g., Ferrarese 2002; Kormendy & Bender 2011; Beifiori et al. 2012), which is the rotational velocity measured at large radius to probe the dark matter halos potential. It is intriguing that these power-law relations, especially the M_{BH}–σ_* relation, hold over several orders of magnitude in BH mass with small scatter, even though the BH accounts for only a few thousandths of the mass of the galaxy (e.g., Häring & Rix 2004).

There are a wide array of theories attempting to explain the BH–galaxy scaling relations (e.g., Silk & Rees 1998; Ciotti & Ostriker 2001; Murray et al. 2005; Hopkins et al. 2006; Peng 2007). Two of the most popular models include variants of feedback from active galactic nuclei (AGNs) and scenarios in which merging alone can lead to BH–galaxy scaling laws. In AGN feedback models, the central BH accretes mass and grows until it is massive enough to expel gas from the galaxy potential well and quench its own growth. BH growth in this picture is regulated by the depth of the galaxy potential well (Silk & Rees 1998; Fabian 1999; Di Matteo et al. 2005; Robertson et al. 2006). On the other hand, the pure merging scenario suggests that the correlation between linear quantities, for example, the BH mass M_{BH} and the halo mass M_{DM}, can emerge from a large number of mergers based on the central limit theorem, even without a physical mechanism linking the two (Peng 2007; Hirschmann et al. 2010; Jahnke & Macciò 2011).

Although both the feedback and merging phenomena may occur in galaxy evolution, it is unclear whether either of the mechanisms is essential for establishing the scaling relations. The most important physical scale for feedback is also a matter of debate (Booth & Schaye 2010; Debuhr et al. 2010). Furthermore, we do not know how the AGN output couples to the gas, whether via thermal energy (Silk & Rees 1998) or momentum (Ostriker et al. 2010), nor do we know the average efficiency of the feedback.

Therefore, empirical evidence that distinguishes the relative importance of different physical processes in establishing the scaling relations is key to constructing the coevolution history of BHs and galaxies. In this paper, we investigate the origin of BH–galaxy scaling relations by comparing the M_{BH}–V_c relation with the M_{BH}–σ_* relation. Circular velocity V_c is a good indicator of dark matter halo mass and velocity dispersion σ_* serves as its counterpart on bulge scales. While some AGN feedback scenarios (e.g., Debuhr et al. 2010) suggest that BH mass will be most tightly linked to baryons (as opposed to dark matter), a pure merging scenario suggests that the M_{BH}–M_{DM} (or M_{BH}–V_c) relation should be the cleanest and tightest relation, as it is free from the baryonic physics (e.g., star formation) that occurs during merging. Comparison of the two relations, especially their scatter, can help determine the mechanism that drives BH–galaxy coevolution (Ferrarese 2002; Novak et al. 2006; Kormendy & Bender 2011).

[5] Alfred P. Sloan Fellow.
[6] Current address: Joint Alma Office, Alsonso de Cordova 3107, Vitacura, Santiago, Chile.

Table 1
VLA Observations

Galaxy	Date (UTC)	Flux Cal.	Phase Cal.	$\Delta\theta$ (deg)	$T_{\rm total}$ (minutes)	$T_{\rm scan}$ (minutes)	Antennas	RFI
(1)	(2)	(3)	(4)	(5)	(6)	(7)	(8)	(9)
NGC 1194	2010 Oct 8	3C48	J0323+0534	8.3	212	26.6	22	Yes
NGC 2748	2010 Oct 10	3C147	J0841+7053	6.0	217	24.6	22	No
NGC 2960	2010 Nov 19	3C286	J0943−0819	11.9	210	26.3	25	Yes
NGC 7582	2010 Dec 4/5	3C48	J2326−4027	2.5	200	19.9	23	Yes
UGC 3789	2010 Oct 7	3C147	J0614+6046	8.2	198	22.0	22	No

Notes. Column 1: galaxy name. Column 2: observation date. Column 3: the flux and bandpass calibrator. Column 4: the phase calibrator. Column 5: the angular separation between the source (galaxy) and the phase calibrator. Column 6: total on-source observation time. Column 7: average length of each source scan, which is the separation between two phase calibrator scans. Column 8: number of antennas used in the observation. Some antennas were not used because the *L*-band receiver was not yet installed or because the antenna had unstable or noisy data quality. Column 9: whether or not radio frequency interference (RFI) was found in the data. The RFI was visually inspected and flagged. After the flagging, there was negligible or minor contamination from RFI in the data cube. The most severe case was NGC 1194, where some faint elongated stripes parallel to the galaxy can be seen.

Ferrarese (2002) first proposed that BH mass may correlate with dark matter halo mass, based on the $M_{\rm BH}$–σ_* relation and the correlation between σ_* and $V_{\rm c}$. Later, a number of papers (Pizzella et al. 2005; Courteau et al. 2007; Ho 2007) pointed out that the σ_*–$V_{\rm c}$ relation depends on surface brightness, light concentration, and morphology and suggested that the $M_{\rm BH}$–σ_* relation, not the $M_{\rm BH}$–$V_{\rm c}$ relation, is most fundamental. Kormendy & Bender (2011) compiled a sample of 25 galaxies with both dynamical BH mass measurements and $V_{\rm c}$ from spatially resolved rotation curves. From this direct $M_{\rm BH}$–$V_{\rm c}$ correlation, they concluded that the dark matter halo mass alone cannot determine the BH mass, given that the BH mass can range from $<10^3$–$10^6\ M_\odot$ at a circular velocity of 120 km s^{-1} (for a different view, see Volonteri et al. 2011). Beifiori et al. (2012) also found the scatter in the $M_{\rm BH}$–$V_{\rm c}$ relation to be about twice as large as that in the $M_{\rm BH}$–σ_* relation using a large sample of $M_{\rm BH}$ upper limits from *Hubble Space Telescope* spectra (Beifiori et al. 2009) and $V_{\rm c}$ from unresolved H I linewidth measurements. For a comprehensive review, see Kormendy & Ho (2013).

In this work, we aim to refine the $M_{\rm BH}$–$V_{\rm c}$ statistics. We start with the most up-to-date galaxy sample with dynamically measured BH masses and study all of these that also have spatially resolved circular velocity measurements, predominantly disk galaxies observed with H I. We present five new H I rotation curves measured with the Karl G. Jansky Very Large Array[7] (VLA) during the Expanded Very Large Array (EVLA) construction period. Three of these galaxies have dynamical $M_{\rm BH}$ values measured from the kinematics of water megamasers in sub-parsec disks (Reid et al. 2009; Greene et al. 2010; Kuo et al. 2011). With BH mass errors smaller than 11%, these megamaser measurements are especially useful in constraining the intrinsic scatter of the $M_{\rm BH}$–$V_{\rm c}$ relations. In total, our sample contains 33 galaxies. We assign $V_{\rm c}$ to all galaxies in a consistent way and investigate $V_{\rm c}$ reliability as a function of the spatial extension of the rotation curve. Using only reliable $V_{\rm c}$ measurements at large radius, we quantify the $M_{\rm BH}$–$V_{\rm c}$ correlation and compare it with the $M_{\rm BH}$–σ_* relation. We investigate whether $M_{\rm BH}$ is correlated more tightly with $V_{\rm c}$ or σ_* to discriminate AGN feedback scenarios from those in which merging alone establishes the scaling relations.

[7] The National Radio Astronomy Observatory is a facility of the National Science Foundation operated under cooperative agreement by Associated Universities, Inc.

2. H I OBSERVATIONS

We observed five spiral galaxies in H I with the VLA. The observations were taken in the *L*-band and the C configuration under project 10B−220 between 2010 October and December (for details, see Table 1). The observations used dual circular polarizations and a single spectral window with 256 channels across the 4 MHz (852 km s^{-1}) bandwidth, giving a channel width of 3.3 km s^{-1}. Twenty-one edge channels on each side were flagged due to a higher noise level. Removing these channels did not affect our results since none of the sources had emission in these parts of the band. The full width at half-power of the primary beam is 32′ and the synthesized beam size ranges from 23″ to 52″ depending on the source declination and number of antennas used (Table 2).

The duration of each observation was 5 hr and the on-source time was ∼200 minutes per source. During a track, the gain calibrator was observed for 3–6 minutes every 20–27 minutes, while the flux calibrator was observed once, for 15–23 minutes. The observations were carried out during the EVLA upgrade phase and some of the *L*-band receivers were not yet installed. For the observations of NGC 1194, NGC 2748, and UGC 3789, four antennas were not in the array, three were missing during the NGC 7582 observations, and two were missing during the NGC 2960 track. One additional antenna was flagged out of the dataset for NGC 1194, NGC 2748, NGC 7582, and UGC 3789 for high noise levels. The total number of antennas used was between 22 and 25, as listed in Table 1. Radio frequency interference was found in three observations and the contaminated data were excluded, which account for only a few percent of the data.

Data calibration and image processing were carried out with the Common Astronomical Software Applications (CASA) package. Time averaging of 10 s and on-line flagging were applied before calibration. The amplitude loss due to time averaging is less than 1% according to the VLA Observational Status Summary. The antenna position correction, antenna-based delays, bandpass, phase gain, amplitude gain and flux scale calibrations were carried out consecutively. The minimum acceptable signal-to-noise ratio (S/N) for the bandpass and gain calibration tables was set to 3. The bandpass solutions were solved for each channel, which gave stable solutions with amplitude variations $\lesssim$1%. The phase gain and amplitude gain were solved for each calibrator scan. Gain elevation curves were applied to correct for elevation-dependent amplitude gain due to

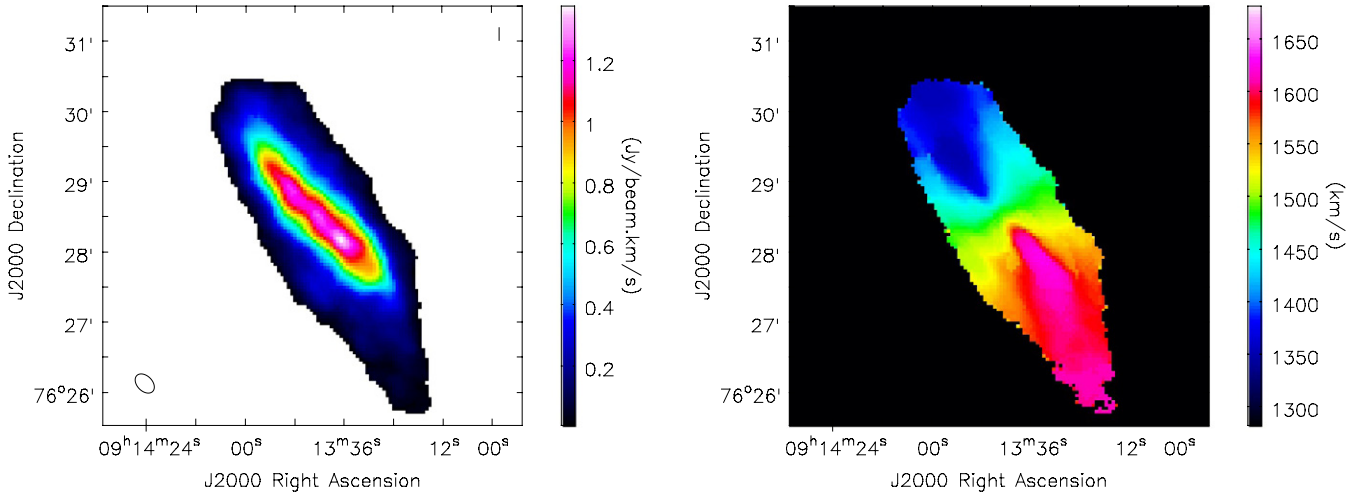

Figure 1. Left: the NGC 2748 moment-0 map made by the CASA *image.moments* tool. The masking is described in Section 3.1. We mask out the pixels below 3σ in a map that is smoothed spatially and over two velocity channels (20 km s^{-1}). We then construct the moment-0 map from the original data using this mask. The ellipse in the bottom left corner represents the beam. Right: NGC 2748 Gaussian/Gauss–Hermite fitted velocity field. Velocity is in optical LSRK.
(A color version of this figure is available in the online journal.)

Table 2
Image Quality

Galaxy	Distance (Mpc)	Channel Width (km s^{-1})	Weighting	Noise (mJy beam^{-1})	Peak (mJy beam^{-1})	Beam FWHM (arcsec×arcsec)	Beam P.A. (deg)	S/N
(1)	(2)	(3)	(4)	(5)	(6)	(7)	(8)	(9)
NGC 2748	24.9	10	Robust = 0.5	0.58	21.98	19 × 13	45	38
NGC 7582	22.3	10	Robust = 0.5	0.81	18.99	52 × 13	0	23
NGC 1194	55.5	20	Natural	0.41	5.80	23 × 16	−2	14
NGC 2960	75.3	20	Natural	0.37	2.29	19 × 18	−14	6
UGC 3789	48.4	20	Natural	0.58	3.42	25 × 16	73	6

Notes. Column 1: galaxy name. Column 2: distance of the galaxy. For consistency, we adopt distances from McConnell & Ma (2013), which are used for the $M_{\rm BH}$ measurements listed in Table 5. Column 3: the binned channel (or image plane) width. The channel width of NGC 2748 and NGC 7582 are set to be smaller because of their higher S/N ratio. Column 4: the imaging weighting method. Column 5: the rms noise level in each image plane measured in line-free channels. Column 6: the peak intensity in the data cube. Column 7: the clean beam FWHM of the major and minor axes. Column 8: the clean beam position angle. Column 9: the S/N ratio, defined by the maximum intensity per channel divided by the rms noise.

antenna deformation. Data weighting was not used throughout the calibration process, since the VLA does not monitor system temperature. The two polarizations were calibrated separately and combined in the imaging process.

For the H I emission line analysis, the continuum was estimated from line-free channels with more than 20 channels on each side and subtracted in the uv plane with the task *uvcontsub*. A constant continuum level was used for all galaxies but NGC 1194 and NGC 2960. In these two galaxies, an adapted linear spectrum was used in order to subtract a nearby bright source with an inclined spectrum. The nearby bright continuum sources were well subtracted at this stage and the contamination from their sidelobes was negligible.

For imaging, we used the CASA task *clean* in *velocity* mode. This mode corrects for the Doppler shift due to the rotation of the Earth. In this process, the channels were also regridded linearly into wider spectral bins—the image planes. The width of the image planes were chosen to be 10 km s^{-1} for higher S/N observations (NGC 2748 and NGC 7582), and 20 km s^{-1} for lower S/N observations (NGC 1194, NGC 2960, and UGC 3789). The S/Ns for each data cube, defined as the peak intensity per channel divided by the rms noise, are listed in Table 2. For NGC 2748 and NGC 7582, we applied Briggs weighting with the parameter *robust* set to 0.5 and natural weighting was applied for NGC 1194, NGC 2960, and UGC 3789. All images were cleaned to the 3σ level. All velocities in this paper use the optical convention and the local standard of rest kinematic (LSRK) reference frame. Position angles (P.A.) in this paper are measured east of north.

3. ANALYSIS

In this section, we describe the procedures that we used to extract velocity fields from the H I data cubes and measure rotation curves and V_c. The H I properties of individual galaxies are discussed in Appendix A.

3.1. Non-parametric Moment-0 and Moment-1 Maps

Non-parametric integrated intensity moment-0 maps of the five galaxies are shown in the left columns of Figures 1–5. In order to improve the S/N, we used the CASA tool *image.moments*, which masked pixels with no signal in producing the moment maps. The masks were produced as follows: the data cube was first smoothed spatially over one beam and spectrally over two image planes (20 km s^{-1} for NGC 2748 and NGC 7582; 40 km s^{-1} for NGC 1194, NGC 2960, and UGC 3789). Then, pixels with smoothed intensity below a

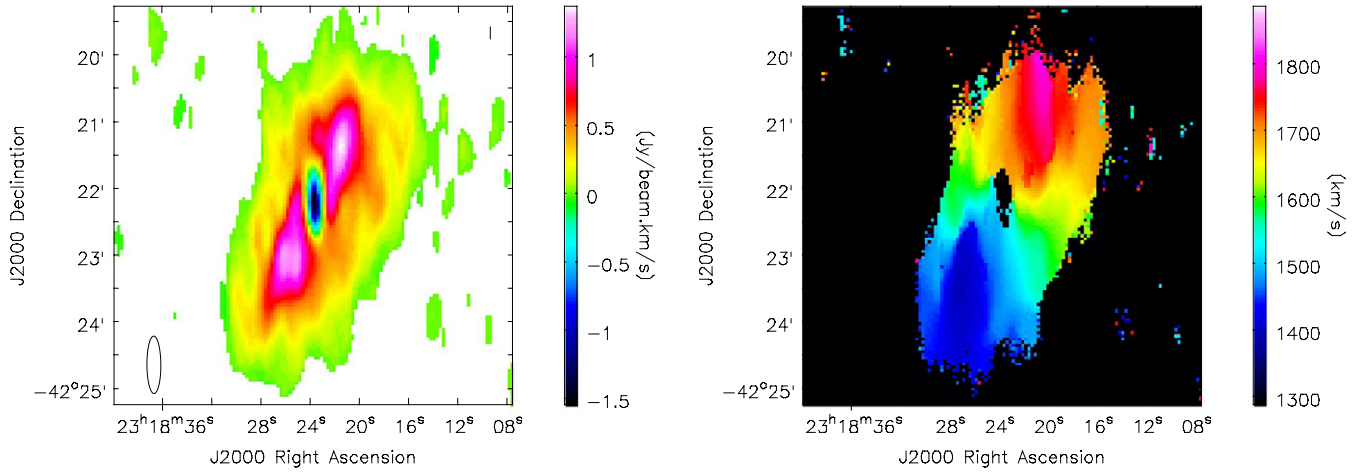

Figure 2. Left: the NGC 7582 moment-0 map. The masking is described in Section 3.1. We mask out the pixels below 3σ in a map that is smoothed spatially and over two velocity channels (20 km s^{-1}). We then construct the moment-0 map from the original data using this mask. The ellipse in the bottom left corner represents the beam. Right: the NGC 7582 Gaussian/Gauss–Hermite fitted velocity field. The central region is masked because of the absorption feature.

(A color version of this figure is available in the online journal.)

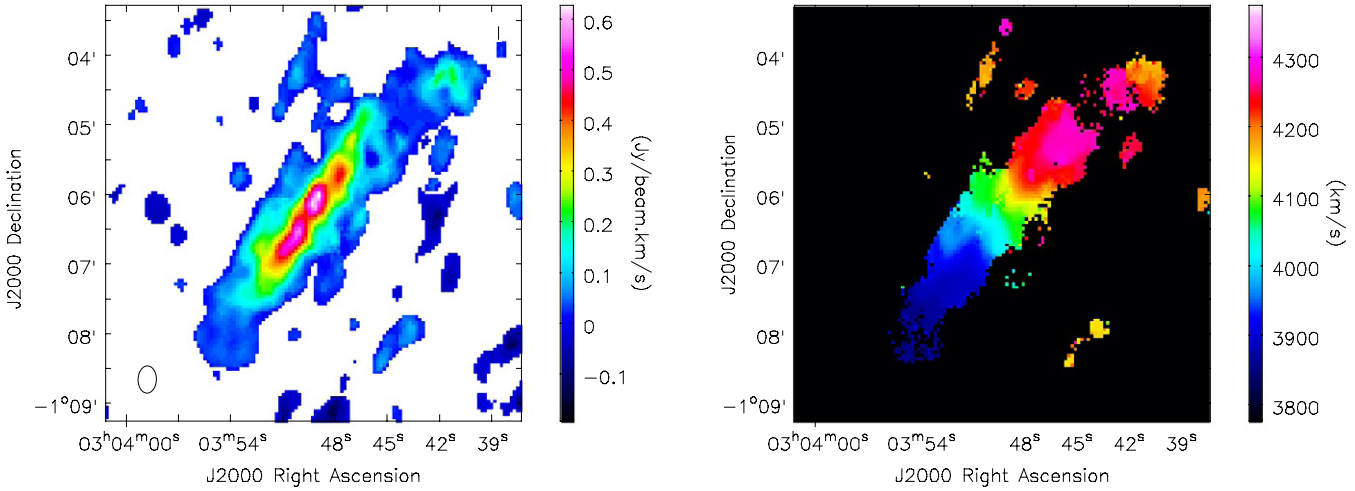

Figure 3. Left: the NGC 1194 moment-0 map. The masking is described in Section 3.1. We mask out the pixels below 2.5σ in a map that is smoothed spatially and over two velocity channels (40 km s^{-1}). We then construct the moment-0 map from the original data using this mask. The ellipse in the bottom left corner represents the beam size. Right: the NGC 1194 Gaussian/Gauss–Hermite fitted velocity field.

(A color version of this figure is available in the online journal.)

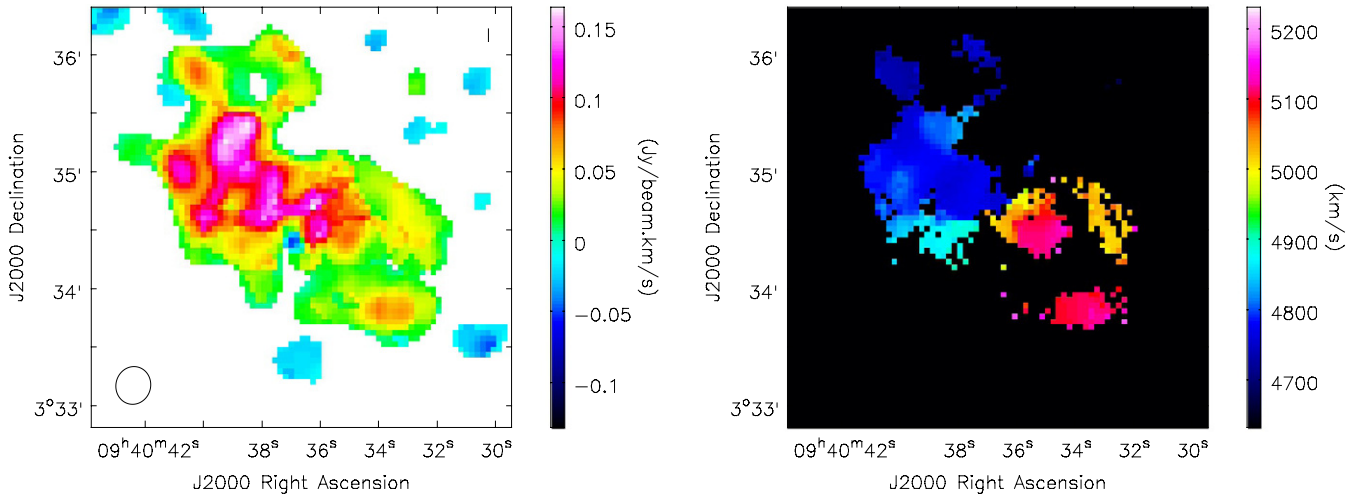

Figure 4. Left: the NGC 2960 moment-0 map. The masking is described in Section 3.1. We mask out the pixels below 2.5σ in a map that is smoothed spatially and over two velocity channels (40 km s^{-1}). We then construct the moment-0 map from the original data using this mask. The ellipse in the bottom left corner represents the beam. Right: the NGC 2960 Gaussian fitted velocity field.

(A color version of this figure is available in the online journal.)

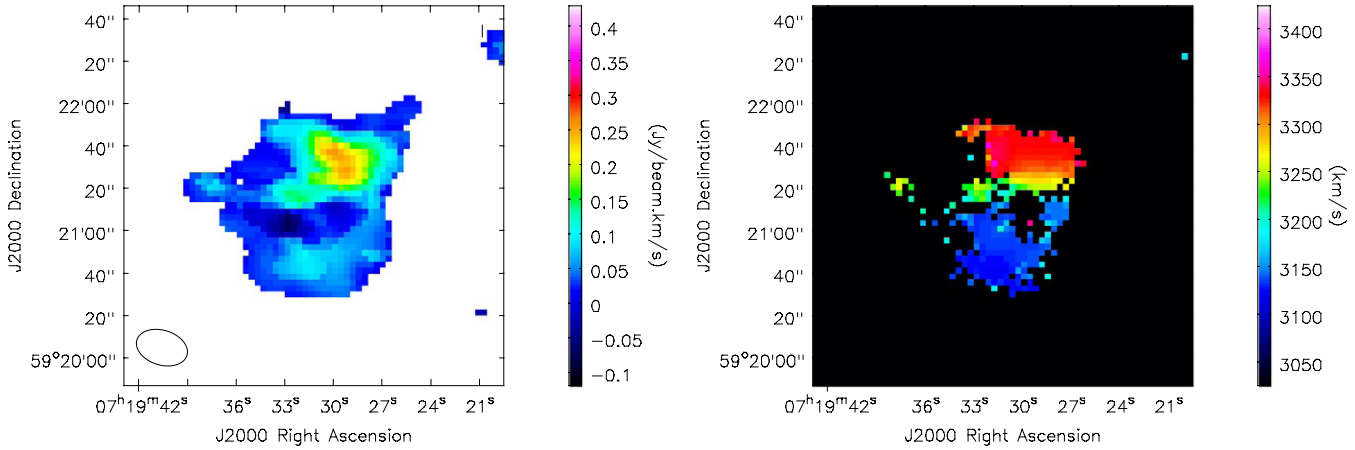

Figure 5. Left: the UGC 3789 moment-0 map. The masking is described in Section 3.1. We mask out the pixels below 2.5σ in a map that is smoothed spatially and over two velocity channels (40 km s^{-1}). We then construct the moment-0 map from the original data using this mask. The ellipse in the bottom left corner represents the beam size. Right: the UGC 3789 Gaussian fitted velocity field.

(A color version of this figure is available in the online journal.)

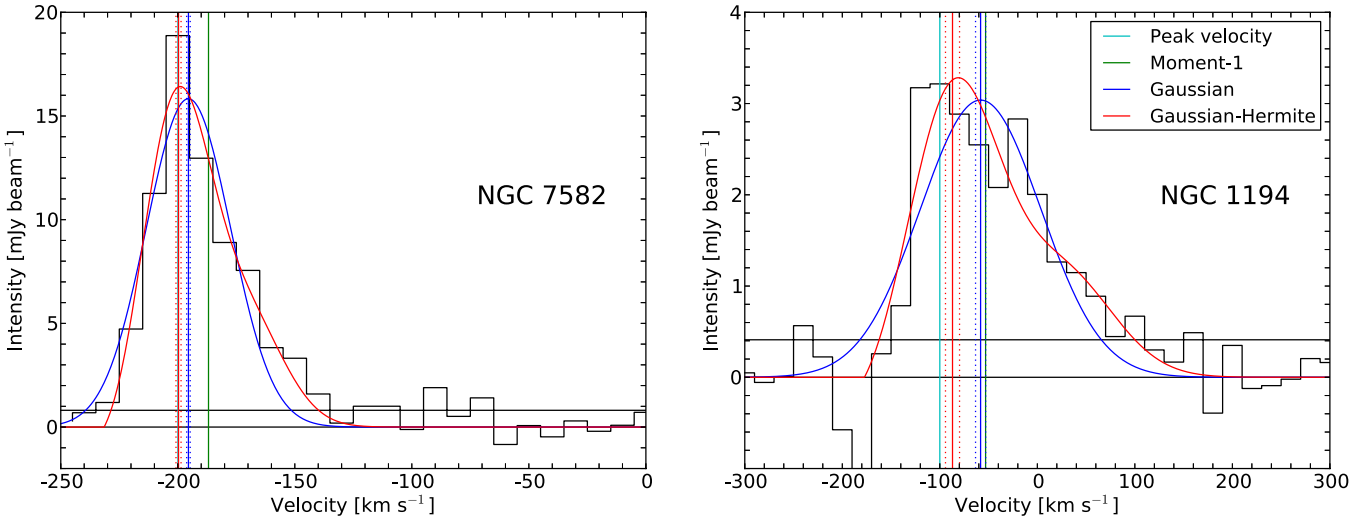

Figure 6. Comparison of different velocity assignments. The cyan vertical line is for peak velocity, green is for moment-1 velocity, blue is for the Gaussian fit, and red is for the Gauss–Hermite fit. Dashed vertical lines are the fitting errors. Black horizontal lines show the 0σ and 1σ intensities. The spectrum on the left is from the NGC 7582 H I data cube, while the one on the right is from the NGC 1194 data cube.

(A color version of this figure is available in the online journal.)

certain threshold were masked. The threshold was set to 3σ for NGC 2748, NGC 7582, and NGC 1194 and 2.5σ for NGC 2960 and UGC 3789, chosen to optimize the signal seen in the moment-0 maps.

3.2. Parametric Fitted Velocity Fields

To extract rotation curves from the H I data cube, it is conventional to fit a velocity-field model. The two-dimensional velocity-field model is parameterized by geometrical parameters and the rotation curve. Then, the model is fit to the two-dimensional velocity field data derived from the three-dimensional data cube. To construct the velocity field, one assigns a representative velocity to each spectrum in the data cube. In the ideal case of a simple rotating disk with small random motions, the projected rotational velocity will correspond to the peak velocity in the spectrum. In practice, there are different ways to measure the velocity at each position, including the peak velocity, the intensity-weighted mean velocity, and parameterized fitting (e.g., Gaussian fitting; deBlok et al. 2008). We seek the velocity measure that can best recover the true projected rotation velocity in the case of finite resolution, sensitivity, disk warping, and overlapping velocities along the line of sight.

Measuring the peak velocity is the most straightforward approach, but the measurement is sensitive to the noise. It may pick up a noise spike instead of the real signal when the S/N is low. Moreover, it is discretized to the velocity channel width, which is 10 or 20 km s^{-1} in our case. The intensity-weighted mean (moment-1) velocity is less sensitive to the noise, but will be biased if the spectrum is not symmetric. For example, beam smearing will produce a wing toward the systemic velocity, causing the intensity-weighted mean velocity to be skewed toward lower values (see the left panel of Figure 6).

Another alternative is parameterized fitting, such as with a Gaussian line profile. The Gaussian fit picks up the intensity peak if the line profile is symmetric and it is not as sensitive to the noise as the peak velocity is, so Gaussian fitting is our preferred approach. However, at high S/N when the line shape is asymmetric, the mean velocity of the best-fit Gaussian profile will be biased toward the wing (see the right panel of Figure 6). In this case, we can use a Gauss–Hermite expansion to capture

the non-Guassian line shape (van der Marel & Franx 1993). For example, the skewness asymmetry is taken into account using the third-order Hermite polynomial $H_3(x)$:

$$x := \frac{v - \bar{v}}{\sigma},$$
$$f(x) = \frac{\gamma}{\sqrt{2\pi}\sigma} \exp\left[-\frac{1}{2}(x)^2\right][1 + h_3 H_3(x)],$$
$$H_3(x) = \frac{1}{\sqrt{6}}(2\sqrt{2}x^3 - 3\sqrt{2}x). \quad (1)$$

Here, the skewness parameter h_3 quantifies the asymmetry of the line shape. The intensity-weighted mean velocity $v_{m,3}$ of this line shape $f(v)$ is calculated by van der Marel & Franx (1993) to be $v_{m,3} = \bar{v} + \sqrt{3}\sigma h_3$ to first order. Compared with a Gaussian, the mean velocity $v_{m,3}$ measured by Gauss–Hermite fitting is less biased toward the wing and closer to the peak, while compared with the peak velocity, the Gauss–Hermite fit is also less sensitive to the noise. Differences in the velocity fields derived from these different methods and their effects on the resulting rotation curves are discussed in Appendix B. We find that for high S/N data, the rotation curve derived from the moment-1 velocity field is systematically lower than from the Gaussian/Gauss–Hermite velocity field at the ∼15% level and that the peak velocity produces noisy rotation curves for low S/N data.

Considering the advantages of Gaussian and Gauss–Hermite fitting, we utilized these two methods to construct the velocity field. In order to minimize contamination from noise, we applied the noise masking described in Section 3.1. We then performed a Markov Chain Monte Carlo (MCMC) fitting of a Gaussian line shape to the five H I data cubes. We assume the likelihood function of intensity is Gaussian and the standard deviation of this Gaussian is a constant throughout the data cube. The standard deviation was measured from the rms intensity of line-free channels in the cube.

For the three highest-S/N galaxies, i.e., NGC 2748, NGC 7582, and NGC 1194 (S/N > 14), there were regions along the major axis with high reduced χ^2 values, i.e., where the cumulative distribution function of χ^2 is larger than 95%, indicating deviations of the line shape from a Gaussian, mostly because of the line asymmetry described above. To better capture the skewness of the line, we fit these high χ^2 spectra with a third-order Gauss–Hermite function. The final velocity fields of NGC 2748, NGC 7582, and NGC 1194 were constructed using a mixture of Gaussian and Gauss–Hermite fitting. The lower S/N cubes of NGC 2960 and UGC 3789 (S/N ∼ 6) do not have enough S/N to show deviations from single Gaussians.

Higher-order deviations from the Gauss–Hermite line shape, such as the fourth-order kurtosis (h_4), still exist in smaller particular regions after using the third-order polynomial; the line-of-sight overlap is severe along the major axis of the edge-on galaxy NGC 1194 and the gas kinematics are complex along the spiral arms in NGC 7582. We did not apply higher-order fits as the inclusion of the H_4 polynomial would not change the mean velocity to the first order (van der Marel & Franx 1993).

One advantage of the MCMC fitting is that the uncertainty in each fitted parameter can be estimated from the standard deviation of the probability distribution probed by the chain. The uncertainties in the velocities are especially useful. A large velocity uncertainty may indicate that the spectrum contains no emission line, only noise. We therefore performed a further masking to exclude pixels with velocity uncertainties larger than 80 km s^{-1}. The final velocity fields are shown in the right panels of Figures 1–5.

Table 3
Fitted Geometric Disk Parameters

Galaxy	x_0 (R.A.)	y_0 (Decl.)	V_{sys} (km s^{-1})	i (deg)	P.A. (deg)
(1)	(2)	(3)	(4)	(5)	(6)
NGC 2748	09^{h}13^{m}43^s.33	+76°28′355″	1482	72.6	35.5
NGC 7582	23^{h}18^{m}23^s.62	−42°22′140″	1588	67.9	153.7
NGC 1194	03^{h}03^{m}49^s.14	−01°06′148″	4075	69.1	142.8
NGC 2960	09^{h}40^{m}36^s.46	+03°34′366″	4939	41.5*	49.5
UGC 3789	07^{h}19^{m}31^s.02	+59°21′179″	3229	43.2*	164.7*

Notes. The rotating-disk model parameters, as described in Section 3.3. Column 1: galaxy name. Columns 2 and 3: center position. For NGC 2748 and NGC 7582, the center position is the fitted H I kinematical center with fitting error ±0.″2. For the megamaser galaxies (NGC 1194, NGC 2960, and UGC 3789), the center is fixed at the maser position (Kuo et al. 2011). Column 4: fitted systemic velocity. The random error from fitting is less than 0.1%, including determining the center for NGC 2748 and NGC 7582, which have no megamaser positions. Column 5: fitted inclination angle, except for NGC 2960 and UGC 3789, which are fixed at HyperLeda values (Paturel et al. 2003). Column 6: fitted P.A., except for UGC 3789, which is fixed at the HyperLeda value (Paturel et al. 2003).

3.3. Rotation Curves

Rotation curves are derived by fitting the velocity fields (Section 3.2) with a rotating disk model. This model consists of coplanar concentric rings, each with its own rotation velocity. The width of each ring is chosen to be 14″, corresponding to the typical beam size. We do not use tilted-ring modeling, but we show in Appendix B that the rotation curves derived with a tilted ring analysis are consistent with those presented here.

The rotation curve fitting was performed with the same MCMC method. We assume that the likelihood function of the velocity is a Gaussian and we use the velocity uncertainty estimated in Section 3.2, such that noisier pixels with larger velocity uncertainties are downweighted naturally. We fit five geometrical parameters, the center x_0, y_0, the systemic velocity v_{sys}, the inclination i, and the P.A., together with the rotation velocity, at each ring. These parameters describe the velocity-field model. For the megamaser galaxies (NGC 1194, NGC 2960, and UGC 3789), we fix the central positions (x_0, y_0) to the VLBI maser positions and we fit the kinematic centers of NGC 2748 and NGC 7582 as free parameters. The v_{sys}, i, P.A., and rotation velocities are fit as free parameters with the exceptions of the inclination in the case of NGC 2960 and UGC 3789 and the P.A. of UGC 3789, where these values could not be constrained by the data. Therefore, we fixed these three values to the HyperLeda values (Paturel et al. 2003), derived from the optical images. The best-fit geometrical parameters are listed in Table 3.

The best-fit rotation curves are plotted in Figure 7. Various error sources in the rotation curves are considered, including the fitting errors estimated by the standard deviation in the Markov chains, the rms errors estimated by the rms variation of the residuals in a ring, and the errors induced by uncertainties in inclination and P.A. It is commonly found that the formal fitting errors in the rotation curve fits are unrealistically small (e.g., deBlok et al. 2008), likely because the rotating disk model fails to capture features in the observed velocity field such that the residuals are non-Gaussian, causing the fitting errors to appear artificially small (5–20 times smaller than the rms error). As shown in Appendix B, the rms error is larger than or

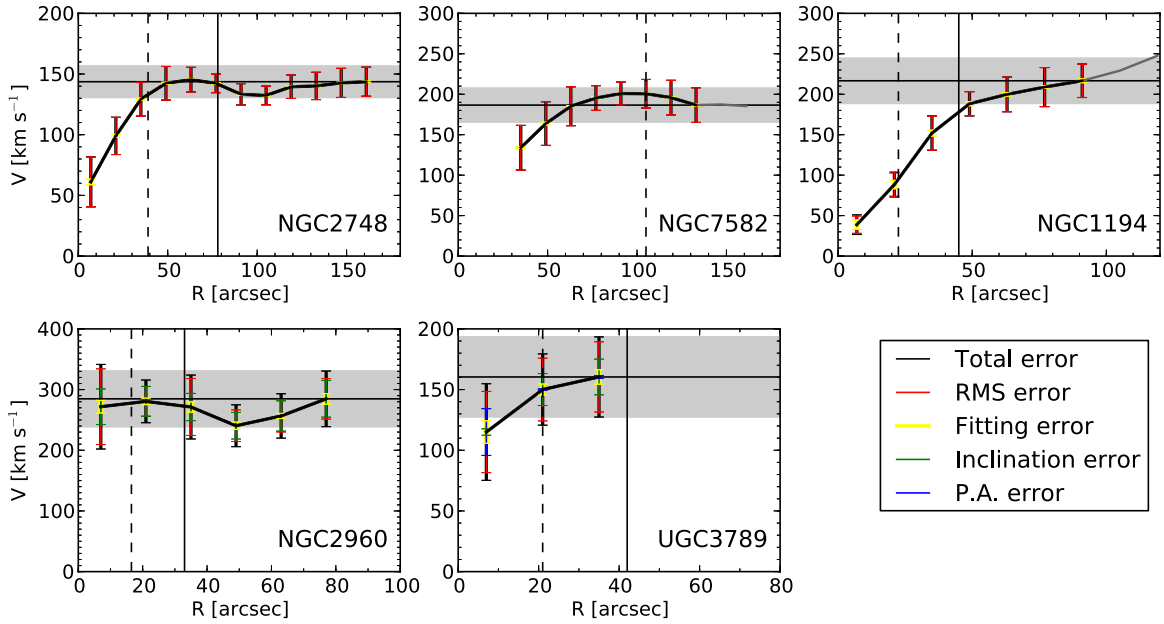

Figure 7. Rotation curves of the five galaxies. Red error bars are the rms errors, which dominate the error budget in all cases. Yellow error bars are the MCMC fitting errors. Green/blue is the error contribution from the inclination/P.A. uncertainty. Black error bars are the total error, calculated by the quadratic sum of all the error sources. The circular velocity V_c, as measured from the outermost radial bin, is denoted by the black horizontal lines with the errors marked with the gray shaded region. This V_c error includes the observational error and the rotation curve variation. The R_{25} radii are marked as the solid black vertical lines and dashed black horizontal lines are $R_{25}/2$. All of the five galaxies have rotation curves extending beyond $R_{25}/2$ and NGC 2748, NGC 1194, and NGC 2960 are beyond R_{25}. For NGC 7582 and NGC 1194, the last two bins, linked by the dark gray lines, are noisy bins and thus not used for the V_c measurements.

(A color version of this figure is available in the online journal.)

comparable with the differences between various velocity assignment methods and different parameterized rotating disk models and therefore provides a conservative estimate of the potential systematic uncertainties. For NGC 2960 and UGC 3789, we also include the uncertainties in the literature inclination and/or P.A. values. The uncertainties contributed by these values are estimated by recalculating the rotation velocities assuming an inclination and/or P.A. within $\pm5^\circ$ of the HyperLeda value. The final error is the quadratic addition of the considered error sources.

4. M_{BH}–V_c RELATION

4.1. The Sample

Our primary sample is an updated list of galaxies with both dynamical M_{BH} and spatially resolved V_c measurements, as tabulated in Tables 4 and 5. There have been a number of compilations of M_{BH} and V_c (Kormendy & Bender 2011; Beifiori et al. 2012); we introduce a few significant improvements over these. First, we update five maser and three stellar/gas dynamical M_{BH} measurements. In addition to our five VLA H I rotation curve V_c measurements, there are a few other V_c measurements included in this sample from the literature that are not compiled in previous M_{BH}–V_c studies. We also reexamine the literature V_c values with a careful reliability analysis, to ensure that our measurements and the literature values are derived in a consistent manner. Thus, our V_c values may differ from previous work. In addition to this primary sample, we also consider a secondary sample composed of galaxies with three spatially unresolved V_c (single-dish H I measurements) and 15 BH mass upper limits. This secondary sample is described in Appendix C and plotted in Figure 8 for comparison, but is not used in our scaling relation fitting analysis.

4.1.1. Circular Velocities V_c

Table 4 lists the V_c values, sources, and rotation-curve properties of our primary sample. We examined each rotation curve from the original literature to assign a V_c value. Because V_c is used as a tracer of the dark matter halo potential in the outer parts of the galaxy, we assign V_c as the rotation velocity at the largest observed radius R_o, which is consistent with the definition in Ferrarese (2002). If the inclination correction is applied in the original literature, we use this inclination-corrected rotational velocity, otherwise we apply a simple $1/\sin(i)$ inclination correction using the optically determined inclination from HyperLeda (Paturel et al. 2003). The uncertainty in V_c that results from our inclination correction treatment is estimated to be less than $\pm10\%$ for a typical inclination error of $\pm5^\circ$ in the optically derived inclination (e.g., Dressler & Sandage 1983) at an average inclination of $\sim60^\circ$. This is comparable with or smaller than the V_c measurement errors described below.

The observational error in V_c, listed first, is taken from the original literature. If it is not presented, then we assume a 10% observational error, which is typical among our sample. The second error stands for the uncertainties due to rotation curve variation. In the ideal case where the rotation curve is flat at large radius, there is one uniquely defined V_c. However, if the rotation curve is not flat but keeps rising or starts to fall, then V_c depends on where the outermost observed radius R_o is located. To take this uncertainty into account, we assign a second error equivalent to the amplitude of variation in the rotation curve. While these error assignments may overestimate the real error between the observed V_c and the true halo potential, we hope to avoid overestimating the intrinsic scatter ϵ_{int} in the M_{BH}–V_c relation. The final error used in the M_{BH}–V_c relation fit is taken as the larger of the observational and rotation curve variation errors, as listed in Table 5.

Table 4
V_c Sources for Primary Sample

Galaxy	V_c (km s^{-1})	V_c Method	V_c Trend	Inc. (deg)	R_o/R_{25}	V_c Reference
(1)	(2)	(3)	(4)	(5)	(6)	(7)
(Group 1) $R_o > R_{25}$						
Circinus	$155 \pm 10 \pm \cdots$	H I	Flat	65	7.5	1
Milky Way	$200 \pm 20 \pm 30$	H I	Oscillating	...	1.3	2
NGC 0224	$230 \pm 15 \pm 50$	H I	Declining	77	1.7	2
NGC 1194	$217 \pm 21 \pm 28$	H I	Slightly rising	69	1.8	...
NGC 1300	$220 \pm 15 \pm 10$	H I	Flat	35	1.6	3
NGC 2273	$190 \pm 8 \pm \cdots$	H I	Flat	55	2.4	4
NGC 2748	$144 \pm 12 \pm 13$	H I	Flat	73	2.0	...
NGC 2787	$222 \pm 5 \pm 15$	H I	Flat	42	4.3	5
NGC 2960	$285 \pm 46 \pm 44$	H I	Oscillating	42	2.1	...
NGC 3031	$180 \pm 10 \pm 50$	H I	Slightly declining	59	1.6	2
NGC 4258	$200 \pm 8 \pm 10$	H I	Slightly oscillating	67	1.8	2
NGC 4736	$115 \pm 5 \pm 55$	H I	Declining	47	1.9	6
NGC 4826	$158 \pm 5 \pm 5$	H I	Oscillating	64	1.9	6
NGC 5128[a]	$308 \pm 20 \pm 61$	H I	Unknown	47	1.2	7
(Group 2) $R_{25} > R_o > R_{25}/2$						
NGC 3227	$247 \pm 5 \pm 10$	H I	Flat	56	0.8	8
NGC 3245	$211 \pm 20 \pm 20$	Optical	Flat	62	0.6	9
NGC 4526	$290 \pm 40 \pm 50$	Optical	Flat	90	0.6	10
NGC 4594	$356 \pm 20 \pm 20$	H I	Flat	85	0.8	11
NGC 4596	$230 \pm 30 \pm 50$	Optical	Flat	38	0.7	12
NGC 7457	$140 \pm 10 \pm 20$	Optical	Rising	73	0.7	9
NGC 7582	$187 \pm 21 \pm 15$	H I	Slightly declining	68	0.6	...
UGC 3789	$160 \pm 33 \pm 10$	H I	Rising	43	0.6	...
(Group 3) Flat $R_{25}/2 > R_o$						
NGC 1023	$256 \pm 30 \pm 0$	Optical	Flat	76	0.5	13
NGC 1332	$229 \pm 20 \pm 10$	Optical	Flat	80	0.4	13
NGC 2549	$102 \pm 10 \pm 13$	Optical	Flat	90	0.4	13
NGC 3115	$315 \pm 10 \pm \cdots$	Optical	Flat	50	0.3	14
NGC 3585	$280 \pm 20 \pm \cdots$	Optical	Flat	90	0.2	15
NGC 4388	$230 \pm 23 \pm \cdots$	H I	Flat	74	0.3	16
NGC 4564	$130 \pm 10 \pm 25$	Optical	Flat	90	0.4	17
(Group 4) Rising $R_{25}/2 > R_o$						
NGC 1068	$283 \pm 58 \pm 60$	Optical	Rising	46	0.5	2
NGC 3384[b]	$177 \pm 16 \pm 56$	Optical	Rising	62	0.2	18
NGC 3998[c]	$285 \pm 40 \pm 57$	H I	Unknown	70	0.5	19
NGC 4026	$170 \pm 10 \pm 30$	Optical	Rising	90	0.5	13

Notes. Circular velocity V_c for the primary sample with both dynamical M_{BH} and rotation curve V_c. Galaxies are grouped according to their spatial extension and rotation curve variation as an indication of V_c reliability. Only Groups 1 and 2 are used to constrain the M_{BH}–V_c relation, while Groups 3 and 4 are excluded, as they may suffer from uncertainties due to short spatial extension. Column 1: galaxy name. Column 2: circular velocity V_c of the galaxy with reference in Column 7. The first error is the observational error. A 10% observational error is assumed if it is not presented in the literature. The second error is the variation of the rotation curve or 20% if the variation is unknown. V_c is evaluated at the outermost radius R_o. Column 3: the observational method of rotation curve measurement. Column 4: radial trends in the rotation curve. Column 5: inclination angle adopted for the V_c inclination correction. If the rotation curve is not inclination-corrected in the literature, the optical inclination from HyperLeda (Paturel et al. 2003) is applied. Column 6: ratio between the outermost radius R_o, at which V_c is evaluated, and the galaxy radius at the B = 25 mag arcsec^{-2} isophote R_{25} from RC2 (de Vaucouleurs et al. 1995). Column 7: references for V_c: (1) Jones et al. 1999; (2) Sofue et al. 1997; (3) Lindblad et al. 1997; (4) Noordermeer et al. 2007; (5) Shostak 1987; (6) deBlok et al. 2008; (7) Schiminovich et al. 1994; (8) Mundell et al. 1995; (9) Cherepashchuk et al. 2010; (10) Pellegrini et al. 1997; (11) Bajaja et al. 1984; (12) Kent 1990; (13) Dressler & Sandage 1983; (14) Bender et al. 1994; (15) Scorza & Bender 1995; (16) Guhathakurta et al. 1988; (17) Halliday et al. 2001; (18) Fisher 1997; (19) Knapp et al. 1985; ($\cdots$) is from this paper.

[a] V_c is estimated from the H I velocity field as the rotation curve is unavailable.

[b] The inclination is estimated by the ratio of the minor/major axes ($\cos i = b/a$) from RC3 (de Vaucouleurs et al. 1991).

[c] V_c was estimated by Knapp et al. (1985) to be 285 ± 40 km s^{-1}, adopting an inclination larger than 70°, while the rotation curve is not available.

There are two galaxies, NGC 3998 and NGC 5128 (Centaurus A), in our primary sample that have no rotation curve measurements but have spatially resolved H I data. For NGC 3998, we adopt the V_c value and observational error estimated by the original literature (Knapp et al. 1985). For NGC 5128, we determine V_c using the published P-V diagram and apply an inclination correction using the inclination from HyperLeda (Paturel et al. 2003). To reflect our lack of

Table 5
M_{BH}–V_c

Galaxy	Morphology	Distance (Mpc)	M_{BH} ($M_\odot$)	M_{BH} Method	σ (km s^{-1})	V_c (km s^{-1})	V_c Method
(1)	(2)	(3)	(4)	(5)	(6)	(7)	(8)
(Group 1) $R_o > R_{25}$							
Circinus	S	4.0	$1.7^{+0.4}_{-0.3} \times 10^6$	Masers	158^{+18}_{-18}	155 ± 10	H I
Milky Way	S	0.008	$4.1^{+0.6}_{-0.6} \times 10^6$	Stars	103^{+20}_{-20}	200 ± 30	H I
NGC 0224	S	0.73	$1.4^{+0.8}_{-0.3} \times 10^8$	Stars	160^{+8}_{-8}	230 ± 50	H I
NGC 1194[a]	S0	55.5	$6.8^{+0.4}_{-0.4} \times 10^7$	Masers	148^{+26}_{-22}	217 ± 28	H I
NGC 1300	S	20.1	$7.1^{+3.4}_{-1.8} \times 10^7$	Gas	218^{+10}_{-10}	220 ± 15	H I
NGC 2273[a]	S	26.8	$7.8^{+0.5}_{-0.5} \times 10^6$	Masers	144^{+18}_{-16}	190 ± 8	H I
NGC 2748[b]	S	24.9	$4.7^{+2.0}_{-1.9} \times 10^7$	Gas	115^{+5}_{-5}	144 ± 13	H I
NGC 2787	S0	7.5	$4.1^{+0.4}_{-0.5} \times 10^7$	Gas	189^{+9}_{-9}	222 ± 15	H I
NGC 2960[a]	S	75.3	$1.21^{+0.07}_{-0.07} \times 10^7$	Masers	166^{+16}_{-15}	285 ± 46	H I
NGC 3031	S	4.1	$8.0^{+2.0}_{-1.1} \times 10^7$	Gas	143^{+7}_{-7}	180 ± 50	H I
NGC 4258	S	7.0	$3.67^{+0.01}_{-0.01} \times 10^7$	Masers	115^{+10}_{-10}	200 ± 10	H I
NGC 4736	S	5.0	$6.8^{+1.6}_{-1.6} \times 10^6$	Stars	112^{+6}_{-6}	115 ± 55	H I
NGC 4826	S	7.3	$1.6^{+0.4}_{-0.4} \times 10^6$	Stars	96^{+5}_{-5}	158 ± 5	H I
NGC 5128	S0/E	4.1	$5.9^{+1.1}_{-1.0} \times 10^7$	Stars	150^{+7}_{-7}	308 ± 61	H I
(Group 2) $R_{25} > R_o > R_{25}/2$							
NGC 3227	S	17.0	$1.5^{+0.5}_{-0.8} \times 10^7$	Stars	133^{+12}_{-12}	247 ± 10	H I
NGC 3245	S0	21.5	$2.1^{+0.5}_{-0.6} \times 10^8$	Gas	205^{+10}_{-10}	211 ± 20	Optical
NGC 4526[c]	S0	16.4	$4.5^{+1.4}_{-1.0} \times 10^8$	Gas	222^{+11}_{-11}	290 ± 50	Optical
NGC 4594	S	10.0	$6.7^{+0.5}_{-0.4} \times 10^8$	Stars	230^{+12}_{-12}	356 ± 20	H I
NGC 4596	S0	18.0	$8.4^{+3.6}_{-2.5} \times 10^7$	Gas	136^{+6}_{-6}	230 ± 50	Optical
NGC 7457[b]	S0	12.2	$8.7^{+5.2}_{-5.2} \times 10^6$	Stars	67^{+3}_{-3}	140 ± 20	Optical
NGC 7582	S	22.3	$5.5^{+1.6}_{-1.1} \times 10^7$	Gas	156^{+19}_{-19}	187 ± 21	H I
UGC 3789[a]	S	48.4	$1.08^{+0.06}_{-0.06} \times 10^7$	Masers	107^{+13}_{-12}	160 ± 33	H I
(Group 3) Flat $R_o < R_{25}/2$							
NGC 1023	S0	10.5	$4.0^{+0.4}_{-0.4} \times 10^7$	Stars	205^{+10}_{-10}	256 ± 30	Optical
NGC 1332	S0	22.7	$1.5^{+0.2}_{-0.2} \times 10^9$	Stars	328^{+16}_{-16}	229 ± 20	Optical
NGC 2549	S0	12.7	$1.4^{+0.1}_{-0.4} \times 10^7$	Stars	145^{+7}_{-7}	102 ± 13	Optical
NGC 3115	S0	9.5	$8.9^{+5.1}_{-2.7} \times 10^8$	Stars	230^{+11}_{-11}	315 ± 10	Optical
NGC 3585	S0	20.6	$3.3^{+1.5}_{-0.6} \times 10^8$	Stars	213^{+10}_{-10}	280 ± 20	Optical
NGC 4388[d]	S	19.8	$8.8^{+1.0}_{-1.0} \times 10^6$	Masers	107^{+8}_{-7}	230 ± 23	H I
NGC 4564	S0	15.9	$8.8^{+2.4}_{-2.4} \times 10^7$	Stars	162^{+8}_{-8}	130 ± 25	Optical
(Group 4) Rising $R_o < R_{25}/2$							
NGC 1068[b]	S	15.4	$8.6^{+0.3}_{-0.3} \times 10^6$	Masers	151^{+7}_{-7}	283 ± 60	Optical
NGC 3384	E	11.5	$1.1^{+0.5}_{-0.5} \times 10^7$	Stars	143^{+7}_{-7}	156 ± 50	Optical
NGC 3998	S0	14.3	$8.5^{+0.7}_{-0.7} \times 10^8$	Stars	272^{+14}_{-14}	285 ± 57	H I
NGC 4026	S0	13.4	$1.8^{+0.6}_{-0.3} \times 10^8$	Stars	180^{+9}_{-9}	170 ± 30	Optical

Notes. Black hole masses, stellar velocity dispersions, and circular velocities of our primary sample. These quantities are plotted in Figure 8 with error bars symmetrized in log space. Column 1: galaxy name. Column 2: morphology. Column 3: distance. Column 4: BH mass measured by method in Column 5. Column 6: stellar velocity dispersion. Columns 2–6 are taken from McConnell & Ma (2013), unless otherwise noted. Column 7: circular velocity with error taken as the larger one of the observational or rotation curve variation error; for more details, see Table 4. Column 8: method of V_c observation.

[a] BH mass uncertainty of 6%, which is dominated by the error of the distance, is adopted, as suggested in Kuo et al. (2011). Note that this error is different from what is listed in McConnell & Ma (2013).

[b] These BH mass measurements are noted in McConnell & Ma (2013) as complicated and are excluded in their paper. More discussion and the M_{BH} references can be found in Section 4.1.2.

[c] The BH mass is from Davis et al. (2013) using molecular gas dynamics.

[d] Same as footnote "a," but a BH mass uncertainty of 11% is adopted.

knowledge about the rotation curve trends, we assign conservative rotation curve variation errors of 20% in these two cases.

How faithfully V_c reflects the potential of the dark matter halo depends on whether the rotation curve is probing the halo-dominated part of the galaxy. Therefore, we compare the outermost observed radius of the rotation curve R_o with the optically determined R_{25}, which is the $B = 25$ mag arcsec^{-2} isophote from RC2 (de Vaucouleurs et al. 1995) shown in

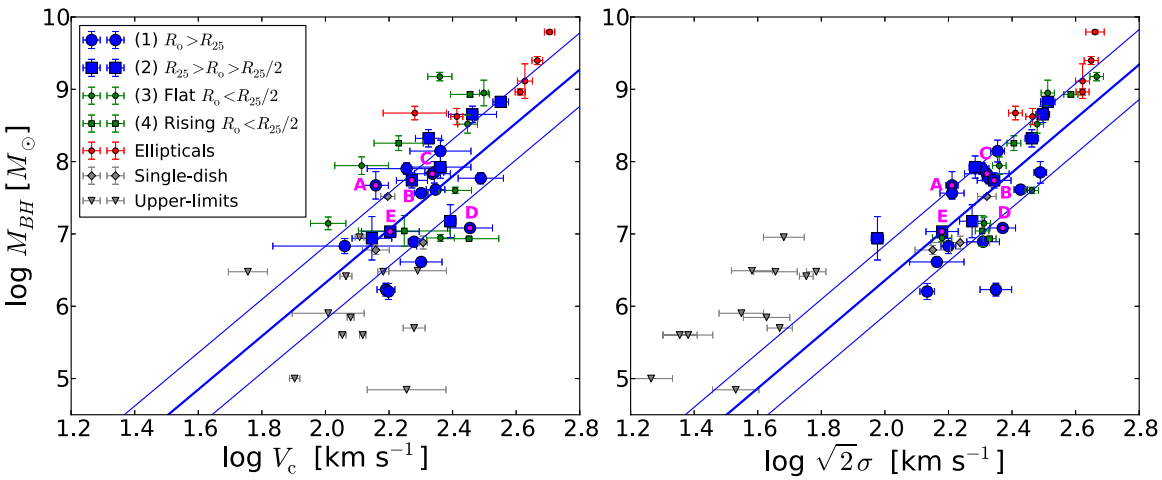

Figure 8. $M_{\rm BH}$–$V_{\rm c}$ (left) and $M_{\rm BH}$–σ_* (right) relations. The data are described in Section 4 and listed in Table 5. Our primary sample with dynamical $M_{\rm BH}$ and spatially resolved $V_{\rm c}$ measurements is plotted in blue or green depending on the rotation curve extent. The blue circles ($R_{\rm o} > R_{25}$) and blue squares ($R_{25} > R_{\rm o} > R_{25}/2$) have long rotation curves and are used for constraining the two relations. The green circles/squares have short rotation curves ($R_{\rm o} < R_{25}$) with flat/rising trends. They are not used to constrain the two relations because of their lower reliability, reflected by the larger scatter in the $M_{\rm BH}$–$V_{\rm c}$ relation. Also plotted is our secondary sample described in Appendix C and listed in Table 9. The gray diamonds and triangles represent the single-dish $V_{\rm c}$ measurements and $M_{\rm BH}$ upper limits, respectively. The red circles are the elliptical galaxies with $V_{\rm c}$ measured by dynamical modeling and $M_{\rm BH}$ from McConnell & Ma (2013), as discussed in Section 4.3. Our five observed H I galaxies are marked by magenta dots labeled as A (NGC 2748), B (NGC 7582), C (NGC 1194), D (NGC 2960), and E (UGC 3789). The fitted $M_{\rm BH}$–$V_{\rm c}$ and $M_{\rm BH}$–σ_* scaling relations using the $R_{\rm o} > R_{25}/2$ primary sample, plotted in blue, are shown by the thick blue line with the intrinsic scatter plotted by the two thin lines. We use $\sqrt{2}\sigma_*$ for the abscissa of the $M_{\rm BH}$–σ_* relation as a direct comparison to $V_{\rm c}$.

(A color version of this figure is available in the online journal.)

Column 6 of Table 4. It is worth noting that if $R_{\rm o}/R_{25}$ is small, as is the case in many optical rotation curves, then the rotation curve may be dominated by baryons rather than the dark matter halo, in turn biasing our measurement of intrinsic scatter in the $M_{\rm BH}$–$V_{\rm c}$ relation. Thus, we divide galaxies into four groups according to the spatial extent and shape of their rotation curves. The first group has the largest spatial extent ($R_{\rm o} > R_{25}$), followed by the second group ($R_{25} > R_{\rm o} > R_{25}/2$). The third and fourth groups both have short rotation curves ($R_{\rm o} < R_{25}/2$), but in the third group the rotation curves flatten while those ones in the fourth group are still rising until the last bin. We discuss the reliability of the $V_{\rm c}$ measurements for these groups in Section 4.3 and conclude that only the first two groups ($R_{\rm o} > R_{25}/2$) have reliable $V_{\rm c}$ values for our $M_{\rm BH}$–$V_{\rm c}$ analysis.

4.1.2. The $M_{\rm BH}$–$V_{\rm c}$ and $M_{\rm BH}$–σ_* Samples

Table 5 lists $V_{\rm c}$, $M_{\rm BH}$, σ_*, and other galaxy quantities. The BH mass $M_{\rm BH}$, stellar velocity dispersion σ_*, morphology, and distance are adopted from McConnell & Ma (2013), except for NGC 4526 (Davis et al. 2013). The method of $M_{\rm BH}$ measurement is also listed. We note potential caveats in the $M_{\rm BH}$ measurements of three galaxies, as pointed out by McConnell & Ma (2013). Lodato & Bertin (2003) measured the BH mass in NGC 1068 and found a non-Keplerian maser disk. For NGC 2748, Atkinson et al. (2005) caution that the determination of the disk center may be affected by heavy extinction. Finally, the BH mass in NGC 7457 as measured by Gebhardt et al. (2003) could be overestimated if the central bright source excluded in their dynamical modeling is a nuclear cluster instead of an AGN. While we keep these three galaxies in our sample, we note these points of caution. The σ_* that we adopt from McConnell & Ma (2013) is the light-weighted stellar velocity dispersion within one effective radius. However, for some galaxies, the σ_* is lower than in previous studies (e.g., Gültekin et al. 2009; Beifiori et al. 2012), as the BH sphere of influence is excluded in the velocity integration to avoid contamination. NGC 3998 and NGC 4594 in our primary sample, as well as NGC 1399 and NGC 4486 in our secondary sample, have σ_* updated by McConnell & Ma (2013) with this correction. We also note that there is a new distance update from megamaser measurements for UGC 3789 (Reid et al. 2013), but we adopt the distance in McConnell & Ma (2013), which is consistent with Reid et al. (2013).

4.2. Fitting Method

To quantitatively analyze the $M_{\rm BH}$–$V_{\rm c}$ and $M_{\rm BH}$–σ_* relations, we fit each scaling relation with a power-law functional form

$$\log(M_{\rm BH}/M_\odot) = \alpha + \beta \log(V_{\rm c}/200\ {\rm km\ s^{-1}}), \quad (2)$$

$$\log(M_{\rm BH}/M_\odot) = \alpha + \beta \log(\sqrt{2}\sigma_*/200\ {\rm km\ s^{-1}}). \quad (3)$$

Here, α is the intercept and β is the logarithmic slope of the relation. We use $\sqrt{2}\sigma_*$ to compare with $V_{\rm c}$, motivated by the widely used singular isothermal sphere model where $V_{\rm c} = \sqrt{2}\sigma_*$ (Binney & Tremaine 2008). Observationally, Ferrarese (2002) also found an almost linear relation between $V_{\rm c}$ and σ with a ratio close to $\sqrt{2}$.

We use a maximum likelihood fitting method similar to Gültekin et al. (2009) that takes intrinsic (or cosmic) scatter $\epsilon_{\rm int}$ into account, with modifications regarding the $V_{\rm c}$ error treatment. For simplicity, we assume that the probability distribution of both the observational errors and intrinsic scatter are normal in log space and all the observational errors are symmetrized in log space before fitting. Here, we denote

$$\mu_i = \log(M_{{\rm BH},i}/M_\odot), \quad (4)$$

$$\nu_i = \log(V_{{\rm c},i}/200\ {\rm km\ s^{-1}}) \quad (5)$$

$$\text{or } \log(\sqrt{2}\sigma_{*,i}/200\ {\rm km\ s^{-1}}), \quad (6)$$

Table 6
Fitted Scaling Relations

x (1)	Sample (2)	Criterion (3)	n (4)	α (5)	β (6)	$\epsilon_{\rm int}$ (7)
$V_{\rm c}$	Group 1, 2	$R_{\rm o} > R_{25}/2$	22	$7.43^{+0.13}_{-0.13}$	$3.68^{+1.23}_{-1.20}$	$0.51^{+0.11}_{-0.09}$
$\sqrt{2}\sigma$	Group 1, 2	$R_{\rm o} > R_{25}/2$	22	$7.48^{+0.11}_{-0.11}$	$3.73^{+0.87}_{-0.89}$	$0.48^{+0.10}_{-0.08}$
$V_{\rm c}$	Group 1	$R_{\rm o} > R_{25}$	14	$7.30^{+0.16}_{-0.15}$	$2.39^{+1.79}_{-1.49}$	$0.53^{+0.14}_{-0.11}$
$V_{\rm c}$	Group 1, 2, 3	$R_{\rm o} > R_{25}/2$ or Flat	29	$7.59^{+0.12}_{-0.12}$	$3.01^{+1.02}_{-0.97}$	$0.62^{+0.10}_{-0.08}$
$V_{\rm c}$	Group 1, 2, 3, 4	All primary sample	33	$7.61^{+0.12}_{-0.12}$	$2.86^{+0.99}_{-0.94}$	$0.65^{+0.1}_{-0.08}$

Notes. Best-fit $M_{\rm BH}$–$V_{\rm c}$ and $M_{\rm BH}$–σ_* scaling relations with model $\log(M_{\rm BH}/M_\odot) = \alpha + \beta \log(x/200\ {\rm km\ s^{-1}})$ of different samples. The first two rows include only galaxies with measured rotation curves extending beyond $R_{\rm o} > R_{25}/2$ and are used for our $M_{\rm BH}$–$V_{\rm c}$ to $M_{\rm BH}$–σ_* comparison. Column 1: the x axis of the relation. Columns 2–3: the sample and the sample criterion used in fitting; see Table 4. Column 4: number of galaxies in the sample. Column 5: best-fit intercept α. Column 6: slope β. Column 7: intrinsic scatter $\epsilon_{\rm int}$.

and the normalized Gaussian error distribution to be $G_\epsilon(x)$ with mean zero and standard deviation ϵ.

To take the error in the independent variable ($V_{\rm c}$ and σ_* in this case) into account, we have an error term σ_ν in the likelihood function. We write the likelihood for observing one galaxy (μ_i, ν_i) given an intrinsic scaling relation $\mu = \alpha + \beta\nu$ with intrinsic scatter $\epsilon_{\rm int}$ to be

$$l_i = G_{\sqrt{\sigma_\mu^2 + \beta^2\sigma_\nu^2 + \epsilon_{\rm int}^2}}(\mu_i - \alpha - \beta\nu_i). \quad (7)$$

This treatment of the errors in the independent variable is less computationally expensive than the Monte Carlo method used in Gültekin et al. (2009). We then maximize the total likelihood

$$\mathcal{L} = \prod_i l_i \quad (8)$$

to obtain the best-fit scaling relation parameters, the intercept α, the slope β, and the intrinsic scatter $\epsilon_{\rm int}$. This maximum likelihood method is similar to the minimum χ^2 method described in Tremaine et al. (2002), except for the $1/\epsilon\sqrt{2\pi}$ normalization factor of the Gaussian function. We adopt the $\Delta\chi^2 = 1$ confidence limit as an error estimate for the fitted parameters α, β, and $\epsilon_{\rm int}$.

4.3. Fitting Results

We find that $M_{\rm BH}$ is correlated with both $V_{\rm c}$ and σ_*, with Spearman rank correlations of $\rho = 0.62$ (p value 2×10^{-3}) and $\rho = 0.67$ (6×10^{-4}) respectively, for the reliable sample of 22 $R_{\rm o} > R_{25}/2$ galaxies discussed below, meaning that a correlation exists for both of the relations. Using this sample, the best-fit $M_{\rm BH}$–$V_{\rm c}$ relation is $\alpha = 7.43^{+0.13}_{-0.13}$, $\beta = 3.68^{+1.23}_{-1.20}$, and $\epsilon_{\rm int} = 0.51^{+0.11}_{-0.09}$ and is plotted as blue lines in Figure 8. There is no significant correlation between the residuals in the $M_{\rm BH}$–$V_{\rm c}$ relation and σ_* (Spearman $\rho = 0.33$, p value$= 0.13$). The parameters of different $M_{\rm BH}$–$V_{\rm c}$ samples, as well as the comparison with the $M_{\rm BH}$–σ_* relation, are listed in Table 6.

To determine a reliable sample and investigate how the spatial extent of the rotation curves affects the reliability of the $V_{\rm c}$ measurements, we derive the scaling relations using samples with different $R_{\rm o}$ criteria. The first group of 14 galaxies ($R_{\rm o} > R_{25}$) should be the most reliable sample with rotation curves that probe the outer, halo-dominated region of the galaxy. The second sample of eight galaxies ($R_{25} > R_{\rm o} > R_{25}/2$) also gives the same intrinsic scatter as the first group, showing that the $V_{\rm c}$ measurements with $R_{25} > R_{\rm o} > R_{25}/2$ are as reliable as the first group for our purpose. When we include groups three and four, the eleven shorter rotation curves with $R_{\rm o} < R_{25}/2$, which are predominantly measured in the optical, the intrinsic scatter increases significantly. It is a sign that for these short rotation curves the halo potential is not represented by the observed $V_{\rm c}$ and the intrinsic scatter will be inflated artificially if they are included in the analysis. We therefore rely only on the $R_{\rm o} > R_{25}/2$ sample of 22 galaxies from the first two groups for our main scientific discussion.

Using this $R_{\rm o} > R_{25}/2$ sample, the $M_{\rm BH}$–$V_{\rm c}$ relation has an intercept consistent with the $M_{\rm BH}$–σ_* relation, if $V_{\rm c}$ corresponds to $\sqrt{2}\sigma_*$. While the slopes of the $M_{\rm BH}$–$V_{\rm c}$ and $M_{\rm BH}$–σ_* relations are consistent within our sample, our $M_{\rm BH}$–$V_{\rm c}$ relation slope falls on the lower end of reported slopes from studies of the $M_{\rm BH}$–σ_* relation using larger samples (e.g., Gültekin et al. 2009; McConnell & Ma 2013), possibly due to our limited dynamic range. The intrinsic scatter in the $M_{\rm BH}$–$V_{\rm c}$ relation of $\epsilon_{\rm int} = 0.51^{+0.11}_{-0.09}$ is similar to that in the $M_{\rm BH}$–σ_* relation of $\epsilon_{\rm int} = 0.48^{+0.10}_{-0.08}$ when using matched $R_{\rm o} > R_{25}/2$ samples, but is larger than the $M_{\rm BH}$–σ_* relation scatter $\epsilon_{\rm int} = 0.38$ for the entire sample in McConnell & Ma (2013), which includes both early and late-type galaxies. The implications of our fits are discussed in Section 6.

Some elliptical galaxies also have $V_{\rm c}$ measured from dynamical modeling. Although these measurements may involve different systematics than the rotation curve-derived $V_{\rm c}$ for disk galaxies, we plot six such ellipticals from Beifiori et al. (2012) in Figure 8 as an attempt to probe the $M_{\rm BH}$–$V_{\rm c}$ trend at the high mass end. NGC 1399, NGC 3379, NGC 4374, NGC 4472, and NGC 4486 (M87) have $V_{\rm c}$ measured by Kronawitter et al. (2000) using stellar kinematics, while NGC 3608 is measured by Coccato et al. (2009). Note that for NGC 4486 (M87), Kronawitter et al. (2000) measured $V_{\rm c} = 508 \pm 38$ km s^{-1}, while Murphy et al. (2011) measured a much larger $V_{\rm c} = 800^{+75}_{-25}$ km s^{-1}, highlighting the challenges in this method. All the BH masses are from McConnell & Ma (2013). When these ellipticals are added, the slopes of the $M_{\rm BH}$–$V_{\rm c}$ relation and $M_{\rm BH}$–σ_* relation increase significantly (by $\sim 1\sigma$ to $\beta = 5.03^{+0.69}_{-0.75}$ and $\beta = 4.77^{+0.57}_{0.58}$, respectively). McConnell & Ma (2013) found a similar steepening in the $M_{\rm BH}$–σ_* relation when considering both early and late-type galaxies. On the other hand, the intrinsic scatter decreases slightly by about 0.5σ to $\epsilon_{\rm int} = 0.46^{+0.10}_{-0.09}$ and $\epsilon_{\rm int} = 0.45^{+0.08}_{-0.07}$ for the $M_{\rm BH}$–$V_{\rm c}$ and $M_{\rm BH}$–σ_* relations, respectively. These

results will not be used in our scientific discussion, as their interpretation awaits better understanding of the correspondence between the V_c from the dynamical modeling and from H I rotation curves.

4.4. Comparison with the Literature

Volonteri et al. (2011) re-analyzed the 25 galaxies in Kormendy & Bender (2011), which have dynamical M_{BH} measurements and V_c from spatially resolved H I or stellar kinematics, using the methods of Gültekin et al. (2009). They constrained the M_{BH}–V_c relation to have $\alpha = 7.39 \pm 0.14$, $\beta = 4.33 \pm 0.93$, and $\epsilon_{int} = 0.53 \pm 0.10$, consistent with our results.

Beifiori et al. (2012) studied the M_{BH}–V_c relation using 28 galaxies with M_{BH} compiled by Gültekin et al. (2009) and V_c from resolved H I kinematics, unresolved H I line width, or dynamical models of stellar kinematics in early type galaxies. Their M_{BH}–V_c relation parameters are $\alpha = 7.82 \pm 0.15$, $\beta = 3.29 \pm 0.61$, and intrinsic scatter $\epsilon_{int} = 0.51 \pm 0.09$. Their intercept α is different from our result, possibly because more elliptical galaxies were included in their sample. Their fit for the slope has a larger dynamic range because they include more elliptical galaxies, but is still consistent with ours, as is their intrinsic scatter measurement.

5. POSSIBLE SYSTEMATIC UNCERTAINTIES

Intrinsic scatter in the scaling relations provides an important discriminant between different BH scaling relation scenarios. Various observational errors in V_c have been taken into account in Section 4 to avoid contaminating the intrinsic scatter measurement, including the inclination correction, the observational error, rotation curve variations, and the uncertainties due to short rotation curves. Here, we discuss whether other systematic uncertainties, such as sample bias, may affect the interpretation of and the comparison between the M_{BH}–V_c and M_{BH}–σ_* relations. Also, in order to interpret the M_{BH}–M_{DM} relation from the observed M_{BH}–V_c relation, we discuss the scatter that may be introduced in the V_c–M_{DM} conversion. We conclude first that the comparison between the M_{BH}–V_c and the M_{BH}–σ_* relations should be fair even in the face of selection effects and second that the scatter introduced by the V_c–M_{DM} conversion or halo triaxiality is not important compared with other sources of uncertainty.

5.1. Selection Effects

If our sample is subject to selection effects, it may not represent the true distribution of objects. Selection effects may exist for both BH and circular velocity measurements. First, it has been argued that analyses excluding M_{BH} upper limits might be biased toward more massive BHs at a given velocity dispersion, especially for late-type galaxies, since only massive BHs have a sphere of influence large enough to be spatially resolved (Gültekin et al. 2011). Beifiori et al. (2012) include a large number of M_{BH} upper limits in their fits to the M_{BH}–V_c and M_{BH}–σ_* relations, which should be closer to the true distribution. They find a slope β for the M_{BH}–V_c relation consistent with ours, but cannot derive a reliable intrinsic scatter. While concerns over M_{BH} selection biases cannot be excluded definitively, we use the same sample for both M_{BH}–σ_* and M_{BH}–V_c relations, such that if M_{BH} biases exist, they have the same effect on the two relations.

In addition to selecting against low-mass BHs, we also select against galaxies that have no V_c from H I rotation curves, which includes massive elliptical (gas-poor) galaxies and disk galaxies that either have only optical (mostly covering a limited radial distance) or no rotation-curve measurements. With no stellar dynamical V_c measurements for ellipticals, our dynamic range is limited compared with the M_{BH}–σ_* relation in other studies, (e.g., Gültekin et al. 2009; McConnell & Ma 2013). While selection biases in V_c measurements also exist, at least there is no obvious bias on the intrinsic scatter inherent with these selections.

5.2. Uncertainties in Translating V_c to M_{DM}

If we wish to interpret the M_{BH}–V_c relation as a reflection of the underlying M_{BH}–M_{DM} relation, then scatter may be introduced in the conversion from V_c to M_{DM}. To estimate the magnitude of this scatter, we take the Navarro–Frenk–White (NFW; Navarro et al. 1996) model as an example. This model is a mass profile that is parameterized by an inner density ρ_s and a characteristic inner radius r_s or, equivalently, the virial mass M_{vir} and the concentration $c_{vir} \equiv R_{vir}/r_s$. The virial radius R_{vir} is defined as the radius within which the averaged halo density exceeds the background density by a certain factor, the virial mass M_{vir} is the mass enclosed within R_{vir}, and the virial velocity V_{vir} is the rotation velocity at R_{vir}. Because there is a one-to-one correspondence between M_{vir} and V_{vir}, the main uncertainty actually comes from the conversion between V_{vir} at the virial radius (typically a few hundred kiloparsecs) and V_c at the observed radius (typically 10–20 kpc; Ferrarese 2002). The observed V_c is close to the maximum velocity V_{max} occurring at radius $r_{max} \sim 2.16 r_s$, which is a few to a few tens of kiloparsecs. The ratio V_{max}/V_{vir} depends on c_{vir}:

$$\frac{V_{max}}{V_{vir}} = 0.46 \sqrt{\frac{c_{vir}}{\ln(1+c_{vir}) - c_{vir}/(1+c_{vir})}}. \quad (9)$$

The scatter in concentration is estimated by Bullock et al. (2001) and corrected by Wechsler et al. (2002) to be $\Delta \log_{10} c_{vir} = 0.14$ dex, which translates to an error of 0.035 dex in V_{max} or 0.14 dex in M_{BH} for a slope of $\beta = 4$ in the M_{BH}–V_c relation. There is also a weak dependence of concentration on the virial mass, which affects the slope of the M_{BH}–V_c relation in principle.

Additionally, if the halo is not spherically symmetric, as assumed by the NFW profile, but is prolate or triaxial, there will be extra uncertainty in the V_c–M_{DM} conversion. Franx & de Zeeuw (1992) estimate that the low observed scatter in the Tully–Fisher relation constrains the ellipticity of the halo potential in the disk plane to be $\leqslant 0.1$. Triaxiality can at most contribute a scatter of 0.026 dex in V_c or 0.1 dex in M_{BH} in the M_{BH}–V_c relation.

Removing these additional sources of uncertainty in quadrature, assuming that they are uncorrelated, changes the final intrinsic scatter very little (0.48 rather than 0.51). Thus, we conclude that those sources of scatter are small compared with the outstanding measurement uncertainty.

6. DISCUSSION

We will now consider the implications of our new fits for the evolution of BHs and galaxies. In Section 6.1, we hope to gain new insight into whether AGN feedback is required to explain the BH–bulge scaling relations (e.g., Silk & Rees 1998; Hopkins et al. 2006) or whether galaxy merging alone may lead to tight BH–bulge correlations in massive galaxies (e.g., Peng 2007; Jahnke & Macciò 2011). In Section 6.2, we discuss the

implications of $M_{\rm BH}$ upper limits as outliers in the $M_{\rm BH}$–$V_{\rm c}$ relation.

6.1. Does Merging Alone Set the Scaling Relations?

We empirically address the relative importance of feedback and merging by asking which can account for features in the observed $M_{\rm BH}$–$V_{\rm c}$ and $M_{\rm BH}$–σ_* relations. We start by reviewing the expected slope, outlier behavior, and intrinsic scatter of the scaling relations in the context of each scenario. We find that while more theoretical guidance and a larger sample size are needed to make inferences from the outliers and slope measurements, the intrinsic scatter is already an available and useful discriminant between the two scenarios.

In the galaxy merging scenario (Peng 2007; Hirschmann et al. 2010; Jahnke & Macciò 2011), the correlations between $M_{\rm BH}$ and galactic quantities (e.g., M_*, $M_{\rm bulge}$, $M_{\rm DM}$) emerge from a large number of mergers simply by the central limit theorem, even without a physical mechanism linking the two. In the context of this scenario, we expect the following features of the scaling relations. First, as the number of mergers increases and the galaxies grow larger, the scatter between $M_{\rm BH}$ and galaxy properties will decrease and the distribution will converge to a tighter correlation. Therefore, it is expected that the intrinsic scatter $\epsilon_{\rm int}$ will decrease as the number of mergers increases toward larger $V_{\rm c}$ and σ_*. Outliers, with BH masses deviating from a power-law scaling relation, become increasingly unlikely toward higher masses. Second, the logarithmic slope β of the correlation between two linear quantities, e.g., $M_{\rm BH}$ and $M_{\rm DM}$, should be close to unity if the impact of growth via accretion for any component is small. In other words, the average ratio $\langle M_{\rm BH}/M_{\rm DM}\rangle$ should be similar across all masses. If we translate this slope to the $M_{\rm BH}$–$V_{\rm c}$ relation, assuming $M_{\rm DM} \propto V_{\rm c}^{3-3.32}$ (Ferrarese 2002), we should find the slope of the $M_{\rm BH}$–$V_{\rm c}$ relation, β, to be close to 3–3.32, somewhat smaller than, but allowed by, our observations. Lastly, the $M_{\rm BH}$–$M_{\rm DM}$ relation should be tighter than other scaling relations, e.g., the $M_{\rm BH}$–M_* or $M_{\rm BH}$–$M_{\rm bulge}$ relations, because $M_{\rm DM}$ simply adds during merging and does not depend on the baryonic physics that M_* and $M_{\rm bulge}$ are subject to. For example, during merging, extra factors of star formation and disk to bulge conversion have to be considered for the evolution of $M_{\rm bulge}$ and this will make the scatter in the $M_{\rm BH}$–$M_{\rm bulge}$ relation larger than that in the $M_{\rm BH}$–$M_{\rm DM}$ relation, if the baryonic regulation mechanism is not present. However, we note that diffuse dark matter accretion in principle may also enhance the scatter in $M_{\rm DM}$.

Feedback, on the other hand, provides a physical mechanism that couples BH mass directly with the galaxy potential well (e.g., Silk & Rees 1998). If the BH is massive enough, its energy or momentum output can expel gas from its vicinity and quench the further growth of both the BH and the galaxy. This feedback loop sets an upper limit on the BH mass for a given potential well depth, measured by the stellar velocity dispersion σ_* of the bulge or $V_{\rm c}$ of the dark matter halo. However, it is unclear whether this self-regulation process takes place on the scale of the BH sphere of influence, the bulge (Debuhr et al. 2010), or the dark matter halo (Di Matteo et al. 2003; Booth & Schaye 2010). Some predictions of the feedback scenario are as follows. First, the scaling relations form an upper boundary for $M_{\rm BH}$. The BH cannot grow above the relation via accretion (although over-massive BHs could already be in place from massive seeds; Volonteri & Natarajan 2009). Second, the slope of the $M_{\rm BH}$–σ_* or the $M_{\rm BH}$–$V_{\rm c}$ relation is predicted to be five for energy feedback (Silk & Rees 1998) and four for momentum feedback (Murray et al. 2005). Third, the correlation between BH mass and the potential indicator (σ_* or $V_{\rm c}$) on the feedback scale should be tighter than on other scales.

We compare here the statistics of our $V_{\rm c}$ sample with the predictions discussed above regarding the outlier properties, slope, and the intrinsic scatter, respectively. There are no obvious outliers above the $M_{\rm BH}$–$V_{\rm c}$ relation in our sample, possibly due to limited sample size. However, there are bulgeless galaxies with $M_{\rm BH}$ upper limits that are low compared with their $V_{\rm c}$, which will be further discussed in Section 6.2. Regarding the measured slopes, with such limited dynamic range our data are still inadequate to discriminate the two scenarios. Both scenarios are consistent with the wide range of allowed $M_{\rm BH}$–$V_{\rm c}$ slopes ($\beta = 2.48$–4.91).

However, the comparison of intrinsic scatter between the two relations can provide useful constraints on the origin of the scaling relations. Our measurements show that the scatter in the $M_{\rm BH}$–$V_{\rm c}$ relation is similar to that in the $M_{\rm BH}$–σ_* relation, within the errors. It is worth noting that the intrinsic scatter in $M_{\rm BH}$–$V_{\rm c}$, $\epsilon_{\rm int} = 0.51^{+0.11}_{-0.09}$ dex, is a conservatively low estimate, as we have assigned large errors to the $V_{\rm c}$ measurements to account for various observational uncertainties, including inclination uncertainties and rotation curve variations. Even so, we still find a value that is consistent with our measured $M_{\rm BH}$–σ_* scatter, $\epsilon_{\rm int} = 0.48^{+0.10}_{-0.08}$ dex, and that is not smaller than the $M_{\rm BH}$–σ_* intrinsic scatter $\epsilon_{\rm int} = 0.46$ for late-type galaxies constrained by McConnell & Ma (2013) or $\epsilon_{\rm int} = 0.38$ for the entire sample in McConnell & Ma (2013).

We find no evidence that the $M_{\rm BH}$–$V_{\rm c}$ (or $M_{\rm BH}$–$M_{\rm DM}$) relation is significantly tighter than the $M_{\rm BH}$–σ_* relation, in contradiction with naive expectations from the pure merging scenario. Therefore, our result disfavors merging as the only mechanism that ties together BHs and galaxies. Note that we use σ_* to trace the baryonic mass in the bulge, while Jahnke & Macciò (2011) looked at the $M_{\rm BH}$–$M_{\rm bulge}$ relation instead. Unfortunately, observations of $M_{\rm bulge}$ for lower-mass galaxies with dynamical $M_{\rm BH}$ are scarce, so a direct comparison between $M_{\rm BH}$–$M_{\rm DM}$ and $M_{\rm BH}$–$M_{\rm bulge}$ is not yet possible. If the real scatter in the $M_{\rm BH}$–$M_{\rm bulge}$ relation is even smaller than in $M_{\rm BH}$–σ_*, our conclusion is stronger. Even if the scatter in the $M_{\rm BH}$–$M_{\rm bulge}$ relation turns out to be larger than in the $M_{\rm BH}$–σ_* relation, the fact that the scatter in the $M_{\rm BH}$–$V_{\rm c}$ relation is no smaller than that in the $M_{\rm BH}$–σ_* relation still requires (baryonic) mechanisms beyond the pure merging scenario.

On the other hand, if AGN feedback is important in regulating BH growth and it acts primarily on the bulge scale (Debuhr et al. 2010), the smaller intrinsic scatter in the $M_{\rm BH}$–σ_* relation could be explained. We speculate that on top of the correlations formed by merging, feedback further regulates the BH mass according to the bulge potential σ_*, tightens the $M_{\rm BH}$–σ_* relation (not the $M_{\rm BH}$–$V_{\rm c}$ relation), and decreases the intrinsic scatter in a relative sense. Alternatively, other baryonic mechanisms that connect the BH to the bulge, e.g., via feeding of bulge stars onto the accretion disk (Miralda-Escudé & Kollmeier 2005) or star formation-regulated BH growth (Burkert & Silk 2001), could also contribute to the tighter $M_{\rm BH}$–σ_* relation.

6.2. $M_{\rm BH}$ Upper Limits in the Two Scaling Relations

$M_{\rm BH}$ upper limits in bulgeless galaxies have also been used to differentiate the dependence of BH mass on galaxy halos or bulges. Kormendy & Bender (2011) found that $M_{\rm BH}$ cannot be uniquely determined by $V_{\rm c}$. Bulgeless galaxies have low

(or zero) M_{BH} and low σ_* but relatively high V_c. Therefore, σ_* is a better predictor of M_{BH} than is V_c for these galaxies.

We expand the sample of bulgeless galaxies with M_{BH} upper limits by including the measurements from Neumayer & Walcher (2012) in our secondary sample. This sample is described in Appendix D and listed in Tables 8 and 9. As can be seen from Figure 8, there are a few upper limits lying below the M_{BH}–V_c relation but not the M_{BH}–σ_* relation. With a larger number of galaxies, we confirm Kormendy's statement that the halo mass alone does not determine the BH mass.

However, it is also possible that these bulgeless galaxies do not host a massive BH at all. The presence or absence of a BH seed may involve different physical mechanisms than those that couple BHs to galaxies (e.g., Volonteri et al. 2011). In any case, the upper limits strengthen our conclusion that bulge scales matter, likely both in seeding and in BH growth with cosmic time.

7. SUMMARY

We refine the measured M_{BH}–V_c relation and compare it to the M_{BH}–σ_* relation to gain insights into the mechanisms that drive BH scaling relations. We perform VLA observations to measure the circular velocities V_c for five galaxies with dynamical M_{BH} measurements. Together with a thorough literature search, we increase the sample size of galaxies with both M_{BH} and V_c measurements to 33. Twenty-two of these have V_c evaluated at large enough radius ($>R_{25}/2$) to be reliable for our scientific purpose.

With this sample, we constrain the power-law M_{BH}–V_c relation to have an intercept $\alpha = 7.43^{+0.13}_{-0.13}$, slope $\beta = 3.68^{+1.23}_{-1.20}$, and intrinsic scatter $\epsilon_{int} = 0.51^{+0.11}_{-0.09}$. The intrinsic scatter in the M_{BH}–V_c relation is not significantly smaller than that in the M_{BH}–σ_* relation, showing that M_{BH} does not correlate better with dark matter halo mass than with bulge properties. This contradicts naive expectations from pure merging scenarios. Furthermore, we consider a number of M_{BH} upper limits in bulgeless galaxies that lie significantly below the M_{BH}–V_c relation, suggesting that BH masses are better predicted by the bulge, not the halo, either via its seeding or accreting mechanism. We thus suggest that pure merging is not likely to be the only mechanism that drives the scaling relations. AGN feedback may also be an essential ingredient to tighten the correlation between BH mass and bulge properties.

We highlight possible future improvements to this work. First, modeling of the dark matter halo mass distribution, to separate the halo mass from the baryons using both rotation curves and light distributions, can improve the halo mass estimation and better constrain the M_{BH}–M_{DM} relation. Second, V_c measured by stellar dynamical modeling for elliptical galaxies, if proven to be comparable with those from H I rotation curves, can improve the dynamic range and better constrain the slope of the relation. Third, quantitative theoretical predictions for the scaling relations, especially the intrinsic scatter, from both feedback and pure merging scenarios, will enable more direct comparisons with the empirical relations. Ultimately, a large sample unbiased with respect to M_{BH} and V_c, which awaits next-generation telescopes, would be the most ideal dataset for this study.

We thank the referee for a very thorough report that helped us improve this manuscript. We thank K. Gültekin, L. C. Ho, N. McConnell, and K. Jahnke for helpful discussions, M. Strauss for constructive suggestions, and J. Kormendy for providing valuable references. We acknowledge the usage of the HyperLeda database (http://leda.univ-lyon1.fr) and NASA/IPAC Extragalactic Database (http://ned.ipac.caltech.edu).

Table 7
H I and Optical Properties

Galaxy	F_{HI} (Jy km s^{-1})	M_{HI} (10^9 $M_\odot$)	M_B (mag)	M_{HI}/L_B ($M_\odot$ $L_{\odot B}^{-1}$)
(1)	(2)	(3)	(4)	(5)
NGC 2748	37.4 ± 5.4	5.47 ± 1.35	−20.33	0.26
NGC 7582	19.6 ± 2.8	2.30 ± 0.57	−20.70	0.08
NGC 1194	7.14 ± 1.07	5.19 ± 1.30	−20.36	0.24
NGC 2960	2.18 ± 0.28	2.92 ± 0.69	−20.76	0.09
UGC 3789	1.26 ± 0.38	0.70 ± 0.25	−20.50	0.03

Notes. The H I flux, H I mass, and M_{HI/L_B} ratios of our five observed galaxies, described in Appendix A.1. Column 1: galaxy name. Column 2: H I fluxes from our VLA observation. Column 3: inferred H I masses from the flux, adopting distances from McConnell & Ma (2013) as given in Table 2. A distance error of 10% is assumed. Column 4: absolute B-band magnitude corrected for extinction from HyperLeda (Paturel et al. 2003). Column 5: H I mass to B-band luminosity ratio, derived from Columns 3 and 4.

APPENDIX A
H I PROPERTIES OF INDIVIDUAL GALAXIES

In addition to the rotation curves kinematics, there is also rich information about the H I gas properties in our VLA data cubes. We discuss the H I fluxes and masses and the H I properties of each individual galaxy in this section. H I moment maps of these galaxies are shown in Figures 1–5 and the integrated spectra of lower S/N galaxies are shown in Figure 9.

A.1. H I Flux and Mass

The H I fluxes and mass are tabulated in Table 7. We measured the H I flux by integrating the data cube over the spatial regions as shown in the moment-0 maps. To avoid contamination, for NGC 1194, we excluded the northwestern cloud, which is detached from the main galaxy, as seen in the moment-0 map. We also removed the central absorption region in NGC 7582. As an estimate of the H I flux error, we also measured the flux from the masked moment-0 maps, which exclude the noise-dominated channels and therefore can underestimate the total flux. We take the difference between the two as the systematic flux error. The H I masses are calculated using the equation

$$M_{HI} = 2.343 \times 10^5\ M_\odot (1+z) \left(\frac{D_L}{\mathrm{Mpc}}\right)^2 \left(\frac{\int F_v dv}{\mathrm{Jy\ km\ s^{-1}}}\right) \quad \text{(A1)}$$

from Draine (2011). For consistency, we adopt the same distances as those used for the M_{BH} measurements in Section 4.1.2 and Table 2. Distance uncertainties of 10% are assumed and the uncertainties in M_{HI} are propagated from the uncertainties in flux and distance. It is common in the literature to compare the H I mass with the total stellar mass, to understand the gas fractions and available fuel for future star formation. Here, we use the B-band luminosity (L_B) as a proxy for the stellar mass and calculate the H I mass-to-light ratio (M_{HI}/L_B) as a proxy for the H I-to-stellar mass ratio. Using the B-band luminosity from HyperLeda (Paturel et al. 2003), the M_{HI}/L_B ratios of our galaxies range from 3% to 22% (Table 7). This is similar to the range of typical Sa galaxies, which have an average value of

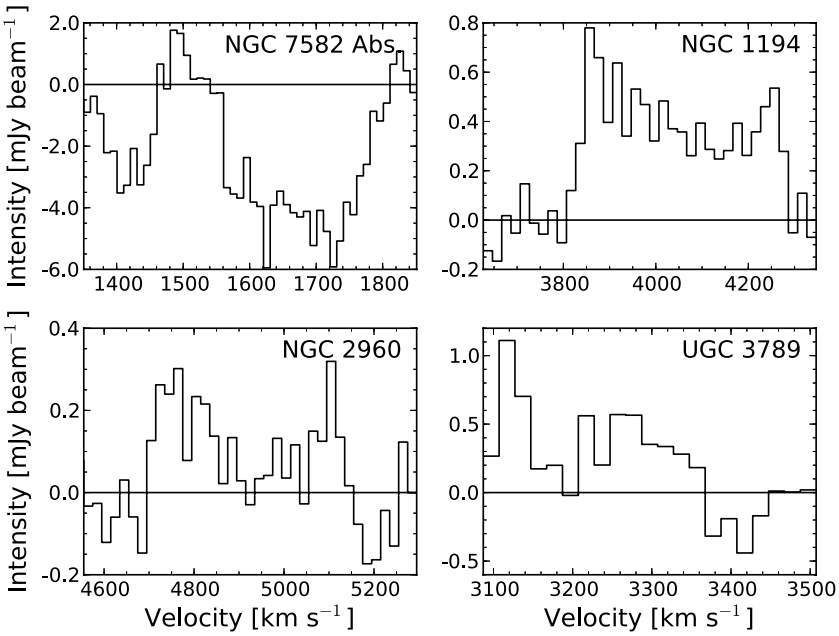

Figure 9. Spectrum of the NGC 7582 central H I absorption feature and the integrated H I emission spectra of the three lower S/N galaxies (NGC 1194, NGC 2960, and UGC 3789).

~10% with a factor of ~3 dispersion (Roberts & Haynes 1994), as well as AGN hosts, which also have $M_{\rm H\,I}/L_{\rm B} \sim 10\%$ (Fabello et al. 2011; Ho et al. 2008). Therefore, our sample galaxies have roughly similar H I-to-stellar mass ratios as typical disk galaxies and AGN hosts.

A.2. NGC 2748

NGC 2748 is an SAbc galaxy (de Vaucouleurs et al. 1991) at a distance of 21.6 ± 1.4 Mpc. The H I observation of this galaxy has the highest S/N among our five galaxies, with an H I-based inclination of 72.°6, compared with 68.°1 from optical data in HyperLeda (Paturel et al. 2003). The fitted H I systemic velocity is 1482 km s^{-1}. The kinematics show the typical signature of a rotating disk (Figure 1). The asymmetric velocity field suggests that slight disk warping may exist. The angular diameter along the major axis at the 3σ level, i.e., where H I is detected above the 3σ level, is 3.′8. The H I flux is measured to be 37 ± 5 Jy km s^{-1}, which corresponds to an H I mass of 4.2 ± 0.9 × 10^9 $M_\odot$.

A.3. NGC 7582

NGC 7582 is an SB(s)ab galaxy (de Vaucouleurs et al. 1991) at a distance of 20.6 ± 2.4 Mpc. Our observation of this galaxy also has high S/N. The inclination derived from the H I kinematics is 67.°9, compared with 68.°2 from HyperLeda (Paturel et al. 2003). The systemic velocity is 1588 km s^{-1}, as fit by H I. Its velocity field shows a clear signature of rotation and is asymmetric (Figure 2), suggesting a warped disk. The velocity discontinuity at the edge of the warp coincides with the location of the spiral arms. Its angular diameter is 3.′7 at the 3σ level. The H I flux is 20 ± 3 Jy km s^{-1}, which corresponds to an H I mass of 2.0 ± 0.5 × 10^9 $M_\odot$.

NGC 7582 shows H I absorption features against the central continuum source. The continuum-subtracted spectrum averaged over the central beam is shown in Figure 9. There is an emission peak at a velocity of 1500 km s^{-1} coinciding in velocity with the emission in nearby regions. Therefore, we suspect that we are observing the superposition of a wide absorption feature with narrow emission. The wide absorption feature has a FWHM of ~ 400 km s^{-1} centered at 1580 km s^{-1}, close to the systemic velocity. Because of contamination from H I emission, we can only estimate a lower limit on the absorbed flux. Using the line width and depth, that flux limit is >0.94 Jy km s^{-1}. The lower limit on the H I absorption optical depth is estimated to be >0.027.

Finally, there are two H I companions of NGC 7582 observed in the same velocity range sitting 9′ and 12′ to the northeast, respectively. These are the companion galaxies NGC 7590 and NGC 7599. There is faint diffuse H I emission ~13′ long that extends from NGC 7590 to the west of NGC 7582 with a closest distance to NGC 7582 of 5.′5. This is possibly tidally stripped gas due to interactions between these galaxies. Larger scale moment-0 and moment-1 maps showing these structures are shown in Figure 10.

A.4. NGC 1194

NGC 1194 is an SA0 galaxy (de Vaucouleurs et al. 1991) at a distance of 53.2 ± 3.7 Mpc. It is one of our water megamaser galaxies (Kuo et al. 2011). The H I S/N is sufficiently high to determine an inclination of 69.°1, compared with 71.°1 from HyperLeda (Paturel et al. 2003). The systemic velocity, as measured from the H I map, is 4075 km s^{-1}. The H I moment-0 map shows an elongated morphology with angular diameter 2.′8 at the 3σ level, showing that the H I gas is organized within the galaxy disk. The velocity field shows a clear velocity gradient due to rotation (Figure 3). The integrated spectrum (Figure 9) also has a clear double peaked rotation signature with the width consistent with our V_c measurement. The H I flux is measured to be 7 ± 1 Jy km s^{-1}, corresponding to a mass of 5 ± 1 × 10^9 $M_\odot$. There is one H I cloud to the northwest side of the galaxy that is detached from the main galaxy body (see Figure 3). This cloud has a mass of 5 ± 2 × 10^8 $M_\odot$.

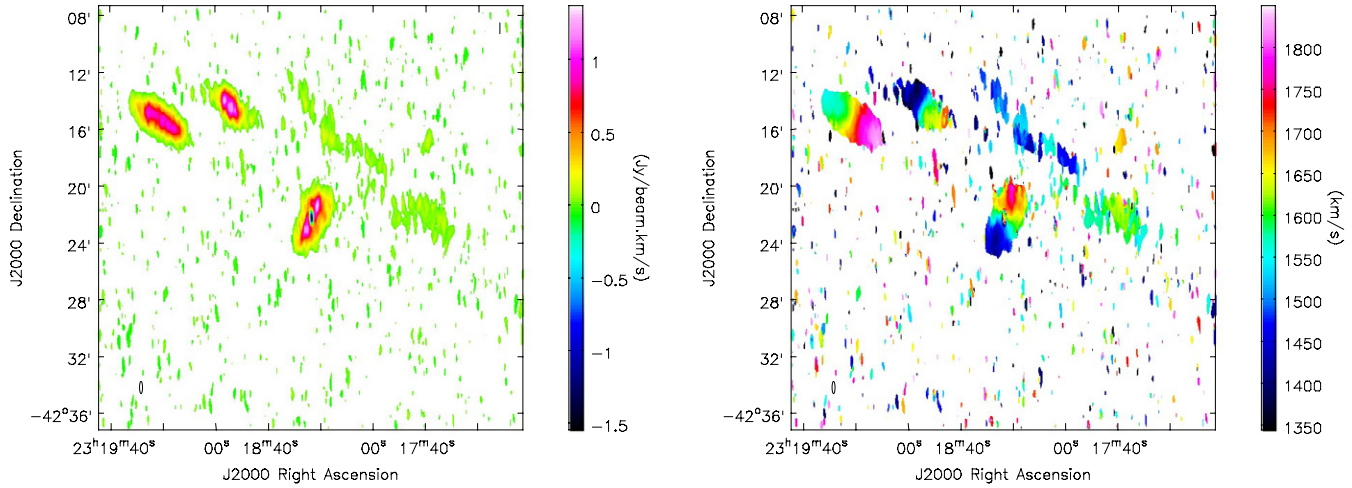

Figure 10. Left: the NGC 7582 moment-0 map on a larger scale. The masking is the same as in Figure 2. We mask out the pixels below 3σ in a map that is smoothed spatially and over two velocity channels (20 km s^{-1}). We then construct the moment-0 map from the original data using this mask. Two companions, NGC 7590 and NGC 7599, and an elongated tidal stream can be seen. Right: the moment-1 map of the same field.

(A color version of this figure is available in the online journal.)

A.5. NGC 2960

NGC 2960, also called Mrk 1419, is an Sa galaxy (de Vaucouleurs et al. 1991) at 72.2 ± 5.1 Mpc and also a water megamaser galaxy from Kuo et al. (2011). The systemic velocity from H I is 4939 km s^{-1}. Our map of NGC 2960 has lower S/N (S/N = 6). Although H I emission is only seen in discrete patches of the galaxy, an overall velocity gradient is observed (Figure 4). The detected diameter is 2.′5 at the 1σ level from the moment-0 map. The inclination cannot be constrained by the H I data alone and we derive the rotation curve by adopting the optical inclination from HyperLeda (Paturel et al. 2003) of 41.°5. The integrated spectrum (Figure 9) shows a double peaked rotation signature and a width that is consistent with our V_c measurement. The H I flux is measured to be 2.2±0.3 Jy km s^{-1}, corresponding to a mass of $2.7 \pm 0.5 \times 10^9$ $M_\odot$. Previous D-array VLA observations (Kuo et al. 2008) are consistent with the spatial extent and velocity from our data, but their H I flux of 1.7 ± 0.3 Jy km s^{-1} is lower than ours. This is understandable as their flux was calculated from the moment-0 map and should be lower than from the data cube.

A.6. Jet in NGC 2960

Our H I data also provide images of the radio continuum at 20 cm. We find that the radio continuum of NGC 2960 is slightly extended, suggesting that there is a radio jet launched from the central BH (Figure 11). The continuum image is made from line-free channels on both sides of the H I line with a total velocity range of 300 km s^{-1} and is cleaned to the 5σ level using $robust = 0.5$ weighting. We measure the size and P.A. of the jet using two different methods. First, we fit a central point source (15.″7) and subtract it. We detect residual emission to the southeast. Taking into account the positional uncertainty due to the finite beamsize, this extended emission is 20″ ± 3″ away from the center at a P.A. of 125°. The flux density in the extended emission is 1.6±0.2 mJy. To estimate the size and P.A. error, we also try a second method to quantify the elongated structure. We fit the entire continuum image with a two-dimensional Gaussian while allowing the semi-major and semi-minor axis, central position, and P.A. to vary, without deconvolution of the beam.

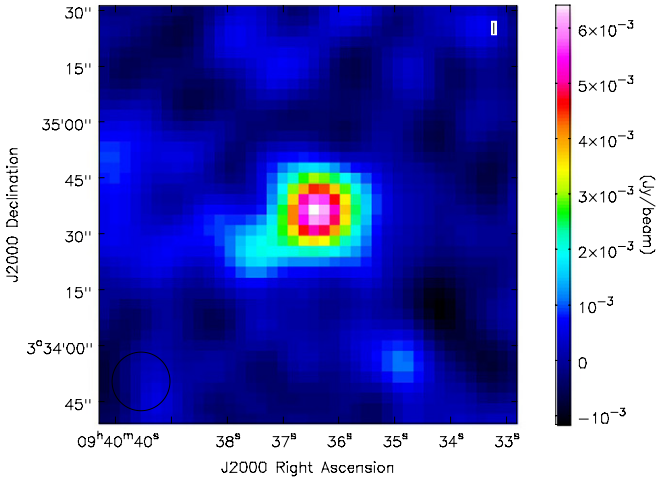

Figure 11. 20 cm continuum image of NGC 2960. There is extended emission on the southwest side of the central point source at the water maser position, suggesting that there is a jet launched from the galaxy nucleus (Appendix A.6).

(A color version of this figure is available in the online journal.)

The fitted Gaussian has a major axis of 22″ ± 4″ and a minor axis of 18″ ± 4″ with P.A. 119° ± 7°, consistent with the first method. Therefore, we conclude that the jet size is 20″ ± 5″ at a P.A. of 125° ± 10°. As in all megamaser galaxies studied to date, the jet axis is coincident with the rotation axis of the maser disk (Greene et al. 2013).

A.7. UGC 3789

UGC 3789 also hosts a water maser disk, is an SA(r)ab galaxy (de Vaucouleurs et al. 1991), and is at a distance of 49.9 ± 7.0 Mpc (Braatz et al. 2010). The H I systemic velocity is 3229 km s^{-1}. The H I observation also has low S/N = 6 and shows a ring-like structure with a diameter of 1.′3 at the 1σ level on the moment-0 map (Figure 5). There is a clear velocity gradient. Neither inclination nor P.A. can be constrained from the H I data alone. The optical inclination i = 43.°2 and P.A. = 164.°7 (Paturel et al. 2003) are adopted to derive the rotation curve. The measured H I flux is 1.3 ± 0.4 Jy km s^{-1},

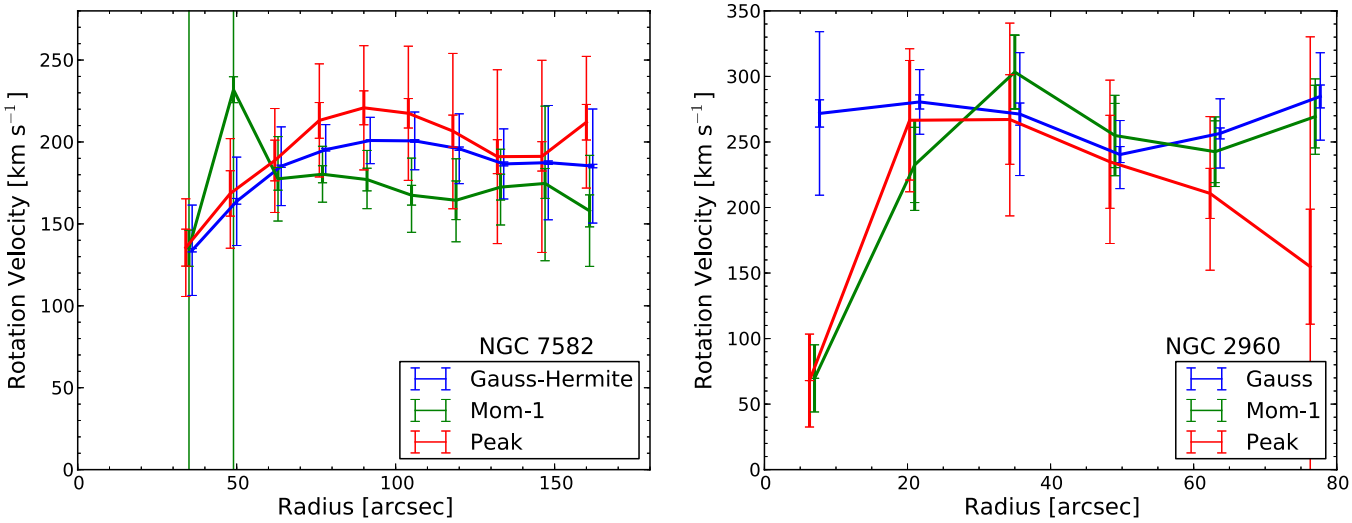

Figure 12. Comparing the rotation curves derived from different velocity fields—Gaussian/Gauss–Hermite (blue), moment-1 (green), and peak velocity (red). The left panel shows NGC 7582 with high S/N = 23 and the right panel shows NGC 2960 with lower S/N = 6. The thick error bars represent the fitted error and the thin error bars are the rms error. NGC 7582 has V_c, the rotation velocity at large radius, from the three velocity fields consistent with each other. However, NGC 2960 has a peak velocity V_c significantly differs from the other two methods. Therefore, the peak velocity may incur large errors in the rotation curves for low S/N data.

(A color version of this figure is available in the online journal.)

corresponding to a mass of $0.7 \pm 0.3 \times 10^9\ M_\odot$. Companion UGC 3797, which is 5′ away to the east, is detected in H I at the same angular distance but we do not detect any H I tidal tails.

APPENDIX B

DETAILS OF ROTATION CURVE ESTIMATION

In this appendix, we investigate two complications that may affect rotation curve estimation. First, we consider differences in rotation curves arising from different methods of assigning velocity. Second, we look at tilted ring modeling, which captures warps in the rotation disk, to see if our circular velocities are changed.

As discussed in Section 3.2, there are various methods to assign velocity to a spectrum, e.g., the peak velocity, the intensity-weighted mean (moment-1), or Gaussian/Gauss–Hermite velocities. The first two methods have some drawbacks. The peak velocity is sensitive to the noise in the data and is discretized to the channel width of the data cube; the moment-1 velocity is biased toward the wing if the spectral line is asymmetric. Our preferred method is therefore the Gaussian/Gauss–Hermite fit. The averaged difference between the Gaussian/Gauss–Hermite and the peak velocity (moment-1) velocity field is 17 (18) km s^{-1} for the high S/N galaxies (NGC 2748, NGC 7582, and NGC 1194) and 37 (33) km s^{-1} for low S/N galaxies (NGC 2960 and UGC 3789).

We now propagate these different velocity assignments to investigate the differences in our inferred rotation curves. We focus on two representative galaxies, NGC 7582 (high S/N = 23) and NGC 2960 (low S/N = 6). We use the same MCMC procedure as discussed in Section 3.3, assuming a homogeneous error in the velocity field of 20 km s^{-1} for NGC 7582 and 40 km s^{-1} for NGC 2960 and applying the same masking as in the Gaussian/Gauss–Hermite velocity field to mask out noisy pixels. The fitted rotation curves are shown in Figure 12. The average differences between the Gaussian/Gauss–Hermite and the peak velocity (moment-1) rotation curves are 11 (23) km s^{-1} for NGC 7582 and 67 (39) km s^{-1} for NGC 2960. Compared with the rms errors of the Gaussian/Gauss–Hermite rotation curves, which are 24 km s^{-1} for NGC 7582 and 37 km s^{-1} for NGC 2960, we found that the peak velocity rotation curve of NGC 7582 is consistent with the Gaussian/Gauss–Hermite rotation curve within the error. However, the peak velocity rotation curve deviates from the Gaussian significantly for the lower S/N galaxy NGC 2960.

These tests confirm our concern that the peak velocity is highly sensitive to noise and is not suitable for estimating the rotation curves for low S/N data. Also, NGC 7582 has a moment-1-derived rotation curve that is systematically lower than the Gaussian/Gauss–Hermite one, with a deviation comparable with the rms error. This is consistent with our expectation that the moment-1 velocity is biased by the wing of the spectral line. Moment-1 velocities usually underestimate the rotation velocity for high S/N data, due to beam smearing and higher intensity at the inner part of the galaxy. This bias was also demonstrated in the left panel of Figure 6. NGC 2690 has a moment-1 rotation curve that differs from the Gaussian rotation curve at a level that is comparable with the rms errors as well. In this case, we see no systematic bias, possibly because the S/N is not high enough to manifest an asymmetric line shape. Considering these effects, we find that the Gaussian/Gauss–Hermite method is relatively reliable in the face of asymmetric line shapes and noisy data.

In Section 3.3, we adopt a coplanar disk model for rotation curve fitting. However, this model does not capture the asymmetry in the velocity field that arises from warping of the disk, as seen in NGC 2748 and NGC 7582. Here, we assess whether these asymmetries have an effect on our V_c estimates. We take our most asymmetric galaxy NGC 7582 as an example and use the *Kinemetry* method (Krajnović et al. 2006) to fit a tilted-ring model. In this model, the P.A. and the inclination of each ring are allowed to vary. Furthermore, second and third-order harmonic terms, e.g., $\sin(2\psi)$ and $\sin(3\psi)$, are included to capture higher frequency variations along each ring. The best-fit models are plotted in Figure 13 with their residuals and the fitted rotation curves are plotted in Figure 14. The tilted-ring model

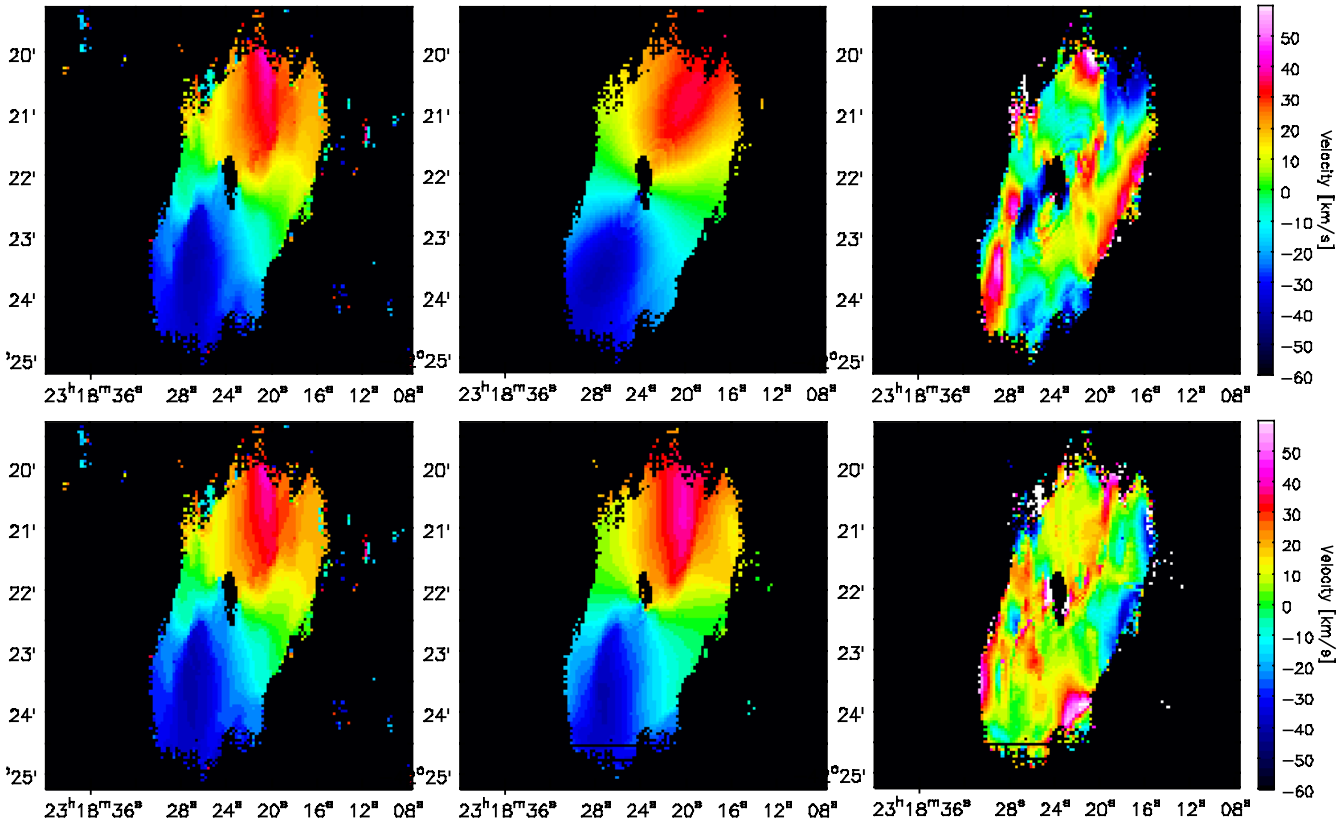

Figure 13. Comparing coplanar (top) and tilted-ring (bottom) models for the velocity field of NGC 7582. From left to right, we show the data (Gauss–Hermite velocity field), the best-fit model, and the residuals. The coplanar model is described in Section 3.3 and the tilted-ring model is described in Appendix B. The color bar represents the color scheme of the residuals. While the tilted-ring model captures the warping feature in the velocity field, we show in Figure 14 that there is very little impact on the inferred rotation curve.

(A color version of this figure is available in the online journal.)

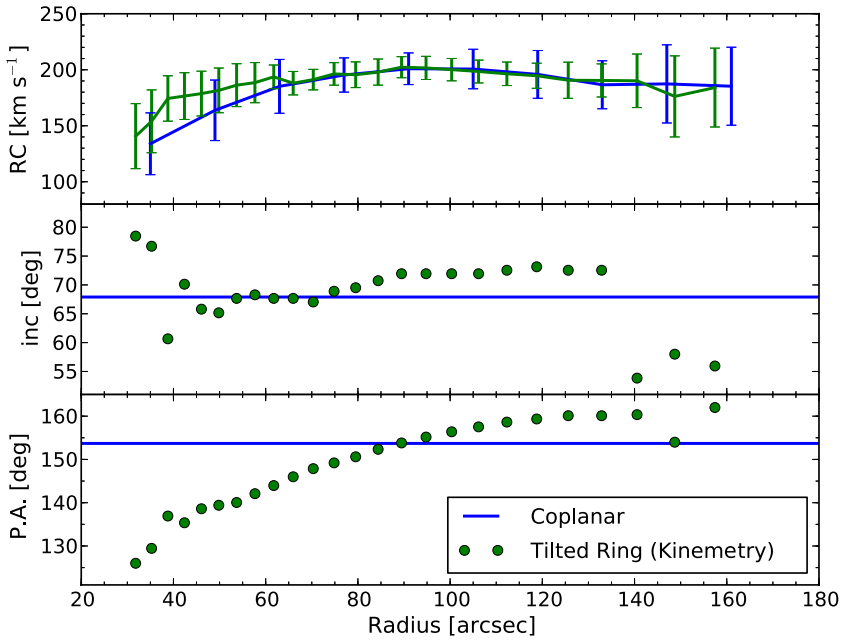

Figure 14. Rotation curves (top), inclinations (middle), and P.A.s (bottom) of the coplanar (blue) and *Kinemetry* tilted-ring (green) models for NGC 7582; for details, see Appendix B and Figure 13. The error bars in the rotation curve measurements represent the rms variation in the residual map. The rotation curves of the two models are consistent with each other within the rms errors, even when the inclination and P.A. of the tilted ring model fluctuate about the coplanar value. The rms errors in the tilted-ring models are smaller than in the coplanar model by 40% between 60″ and 130″, meaning that some of the variations are accounted for by the higher-order terms and the tilted rings of *Kinemetry*.

(A color version of this figure is available in the online journal.)

Table 8
V_c Sources for Secondary Sample

Galaxy	V_c (km s^{-1})	V_c Method	V_c Trend	Inc. (deg)	R_o/R_{25}	V_c Reference
(1)	(2)	(3)	(4)	(5)	(6)	(7)
Dynamical M_{BH} with single-dish V_c						
NGC 3368	203 ± 6	SD	...	49	...	2
NGC 3393	157 ± 8	SD	...	31	...	1
NGC 3489	144 ± 14	SD	...	65	...	2
Upper-limit M_{BH}						
IC 0342	$190 \pm 15 \pm \cdots$	RC	Flat	25	1.6	3
NGC 0205[a]	$26 \pm 3 \pm 5$	*V*-field	Unknown	90	0.2	4
NGC 0300	80 ± 3	SD	...	...	...	2
NGC 0428	$180 \pm 30 \pm 50$	Optical	Oscillating	48	1.3	5
NGC 0598	$135 \pm 13 \pm 35$	RC	Rising	50	1.8	6
NGC 1042	57 ± 8	SD	...	...	...	2
NGC 2139	131 ± 3	SD	...	...	...	2
NGC 3423	120 ± 3	SD	...	...	...	2
NGC 3621	$152 \pm 2 \pm 6$	RC	Flat	65	2.7	7
NGC 5457	$195 \pm 10 \pm 40$	RC	Declining	18	0.5	3
NGC 6503	$116 \pm 2 \pm 5$	RC	Flat	74	1.9	8
NGC 7418	128 ± 4	SD	...	...	...	2
NGC 7424	113 ± 3	SD	...	...	...	2
NGC 7793	$102 \pm 5 \pm 26$	RC	Slightly declining	42	1.3	7

Notes. V_c reliability for the secondary sample. Column 1: galaxy name. Column 2: circular velocity V_c of the galaxy with reference in Column 7. The first error is the observational error. For the rotation curve V_c, the second error is the variation in the rotation curve or 20% if the variation is unknown. For rotation curves, V_c is evaluated at the outermost radius R_o. Column 3: the observational method used to derive V_c. RC stands for spatially resolved rotation curve and SD stands for H I single-dish observation. Column 4: radial trend in the rotation curve. Column 5: inclination used for V_c inclination correction. Column 6: ratio between the outermost radius R_o and the galaxy radius at the B = 25 mag arcsec^{-2} isophote R_{25} from RC2 (de Vaucouleurs et al. 1995). Column 7: references for V_c: (1) HyperLeda (Paturel et al. 2003); (2) Ho 2007; (3) Sofue et al. 1997; (4) Young & Lo 1997; (5) Cherepashchuk et al. 2010; (6) Corbelli & Salucci 2000; (7) deBlok et al. 2008; (8) Begeman et al. 1991.
[a] V_c is estimated from the H I velocity field as a rotation curve is unavailable.

better captures warps in the disk and reduces the residuals, but the best-fit rotation velocities stay unchanged within the uncertainties. The difference at the outermost bin is less than 5% of the rms error. This demonstrates the robustness of the rotation curve fitting against warps and higher-order variations of the velocity field and shows that the rms error is a conservative estimate of the potential systematics in the rotation curve fitting.

APPENDIX C

V_c FROM SINGLE-DISH MEASUREMENTS

In our secondary sample, we have three galaxies (NGC 3368, NGC 3393, NGC 3489) with dynamical M_{BH} but no available rotation curves. However, V_c can also be inferred from the line width of integrated H I spectra taken with single-dish radio observations ($V_{c,SD}$) and the single-dish V_c for these three galaxies from HyperLeda (Paturel et al. 2003) are listed in Table 8.

Since single-dish measurements are more readily available for large samples, they have been used in previous scaling-relation studies (Pizzella et al. 2005; Courteau et al. 2007; Ho 2007; Beifiori et al. 2012). Roberts (1978) and Ho (2007) find that $V_{c,SD}$ is a robust substitute for $V_{c,RC}$. On the other hand, without spatial information, single-dish circular velocities may contain large uncertainties due to the distribution of atomic gas, irregular rotation-curve shape, or contamination from companion galaxies. In general, the values may skew toward lower values, since single-dish measurements are biased to the inner part of the rotation curve.

To understand how much $V_{c,SD}$ can deviate from $V_{c,RC}$, we compare the two numbers for all galaxies in our sample that have both measurements (Figure 15). For most of the galaxies, $V_{c,SD}$ is consistent with $V_{c,RC}$. However, for a few of them, the two numbers can deviate by up to a factor of two. These are preferentially S0 galaxies, suggesting that in these cases low gas fractions are skewing the $V_{c,SD}$ values low. On the other hand, there are only three galaxies in our sample that only have single-dish H I measurements. In practice, including or excluding these three galaxies from our fitting does not change the result. We decide not to include them in our primary sample.

APPENDIX D

M_{BH} UPPER LIMITS

For completeness, dynamically constrained M_{BH} upper limits for bulgeless galaxies, mostly from Neumayer & Walcher (2012), are listed in the second section of Tables 8 and 9. The V_c values are assigned as described in Section 4.1.1, except for the single-dish V_c, which are from HyperLeda (Paturel et al. 2003). These upper limits are also plotted in Figure 8 as gray triangles in both of the scaling relations. Some of them are outliers in the M_{BH}–V_c relation (see the discussion in Section 6.2).

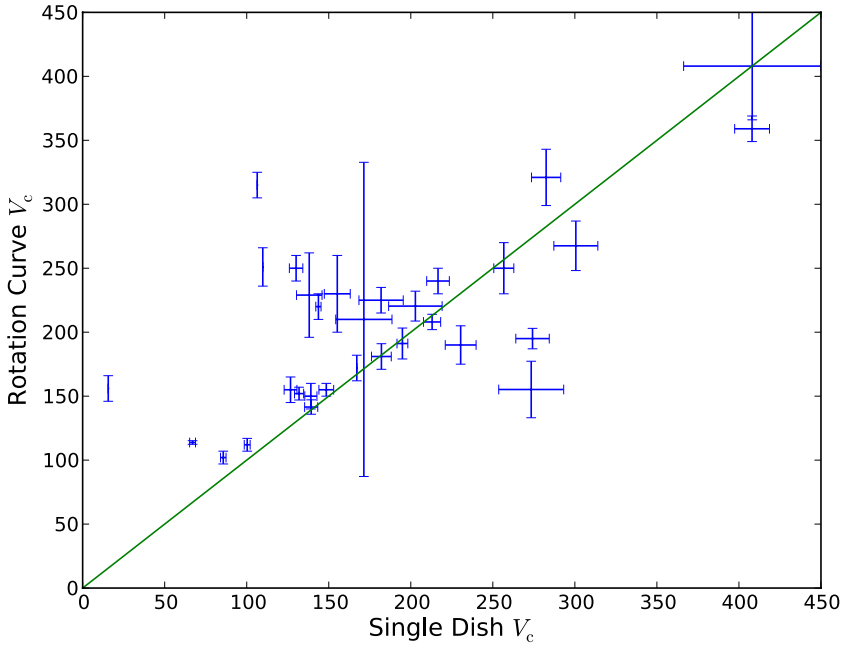

Figure 15. Rotation curve circular velocity vs. single-dish circular velocity for all galaxies in our sample with both. The solid green line represents $V_{c,SD} = V_{c,RC}$. (A color version of this figure is available in the online journal.)

Table 9
M_{BH}–V_c Secondary Sample

Galaxy	Morphology	Distance (Mpc)	M_{BH} ($M_\odot$)	M_{BH} Method	M_{BH} Ref.	σ (km s^{-1})	V_c (km s^{-1})	V_c Method
(1)	(2)	(3)	(4)	(5)	(6)	(7)	(8)	(9)
Dynamical M_{BH} with single-dish V_c								
NGC 3368	S	10.6	$7.6^{+1.6}_{-1.5} \times 10^6$	Stars	1	122^{+28}_{-24}	203 ± 6	SD
NGC 3393	S	53.6	$3.3^{+0.2}_{-0.2} \times 10^7$	Masers	1	148^{+10}_{-10}	157 ± 8	SD
NGC 3489	S0	12.0	$6.0^{+0.8}_{-0.9} \times 10^6$	Stars	1	100^{+15}_{-11}	144 ± 14	SD
Upper-limit M_{BH}								
IC 0342	S	1.8	$<5 \times 10^5$	Stars	2	33 ± 3	190 ± 15	RC
NGC 0205	E (dwarf)	0.74	$<2 \times 10^4$	Stars	3	39 ± 6	26 ± 5	*V*-field
NGC 0300	S	2.2	$<1 \times 10^5$	Stars	4	13 ± 2	80 ± 3	SD
NGC 0428	S	16.1	$<7 \times 10^4$	Stars	4	24 ± 4	180 ± 50	Optical
NGC 0598	S	0.8	$<2 \times 10^3$	Stars	5	19.8 ± 0.8	135 ± 35	RC
NGC 1042	S	18.2	$<3 \times 10^6$	Stars	4	32 ± 5	57 ± 8	SD
NGC 2139	S	23.6	$<4 \times 10^5$	Stars	4	17 ± 3	131 ± 3	SD
NGC 3423	S	14.6	$<7 \times 10^5$	Stars	4	30 ± 5	120 ± 3	SD
NGC 3621	S	6.6	$<3 \times 10^6$	Stars	6	43 ± 3	152 ± 6	RC
NGC 5457	S	7.0	$<3 \times 10^6$	Stars	7	27 ± 4	195 ± 40	RC
NGC 6503	S	5.27	$<3 \times 10^6$	Stars	7	40 ± 2	116 ± 5	RC
NGC 7418	S	18.4	$<9 \times 10^6$	Stars	4	34 ± 5	128 ± 4	SD
NGC 7424	S	10.9	$<4 \times 10^5$	Stars	4	16 ± 2	113 ± 3	SD
NGC 7793	S	3.3	$<8 \times 10^5$	Stars	4	25 ± 4	102 ± 26	RC

Notes. BH masses, stellar velocity dispersions, and circular velocities of our secondary sample for either H I single-dish V_c or upper limits for M_{BH}. These quantities are plotted in Figure 8 in gray with error bars symmetrized in log space. Column 1: galaxy name. Column 2: morphology. Column 3: distance. Column 4: BH mass measured by method. Column 5: method for inferring BH mass. Column 6: reference. Column 7: stellar velocity dispersion. For the first section (single-dish V_c), Columns 2–7 are taken from McConnell & Ma (2013) and original references can be found therein. For the second section (M_{BH} upper limits), Columns 2–3 are from McConnell & Ma (2013) and Columns 4, 5, 7 are from the M_{BH} references listed in Column 6. Column 8: circular velocity with error taken as the larger one of the observational or the RC variation error (see Table 8). Column 9: the observational method of V_c. SD stands for spatially unresolved single-dish V_c, RC for H I rotation curve V_c, H I *V*-field for spatially resolved data but unavailable rotation curves, and optical for optical rotation curves.

References. (1) McConnell & Ma 2013; (2) Böker et al. 1999; (3) Valluri et al. 2005; (4) Neumayer & Walcher 2012; (5) Gebhardt et al. 2001; (6) Barth et al. 2009; (7) Kormendy et al. 2010.

REFERENCES

Atkinson, J. W., Collett, J. L., Marconi, A., et al. 2005, MNRAS, 359, 504
Bajaja, E., van der Burg, G., Faber, S. M., et al. 1984, A&A, 141, 309
Barth, A. J., Strigari, L. E., Bentz, M. C., Greene, J. E., & Ho, L. C. 2009, ApJ, 690, 1031
Begeman, K. G., Broeils, A. H., & Sanders, R. H. 1991, MNRAS, 249, 523
Beifiori, A., Courteau, S., Corsini, E. M., & Zhu, Y. 2012, MNRAS, 419, 2497
Beifiori, A., Sarzi, M., Corsini, E. M., et al. 2009, ApJ, 692, 856
Bender, R., Saglia, R. P., & Gerhard, O. E. 1994, MNRAS, 269, 785
Binney, J., & Tremaine, S. 2008, Galactic Dynamics (2nd ed.; Princeton, NJ: Princeton Univ. Press)
Böker, T., van der Marel, R. P., & Vacca, W. D. 1999, AJ, 118, 831
Booth, C. M., & Schaye, J. 2010, MNRAS, 405, L1
Braatz, J. A., Reid, M. J., Humphreys, E. M. L., et al. 2010, ApJ, 718, 657
Bullock, J. S., Kolatt, T. S., Sigad, Y., et al. 2001, MNRAS, 321, 559
Burkert, A., & Silk, J. 2001, ApJL, 554, L151
Cherepashchuk, A. M., Afanas'ev, V. L., Zasov, A. V., & Katkov, I. Y. 2010, ARep, 54, 578
Ciotti, L., & Ostriker, J. P. 2001, ApJ, 551, 131
Coccato, L., Gerhard, O., Arnaboldi, M., et al. 2009, MNRAS, 394, 1249
Corbelli, E., & Salucci, P. 2000, MNRAS, 311, 441
Courteau, S., McDonald, M., Widrow, L. M., & Holtzman, J. 2007, ApJL, 655, L21
Davis, T. A., Bureau, M., Cappellari, M., Sarzi, M., & Blitz, L. 2013, Natur, 494, 328
deBlok, W. J. G., Walter, F., Brinks, E., et al. 2008, AJ, 136, 2648
Debuhr, J., Quataert, E., Ma, C.-P., & Hopkins, P. 2010, MNRAS, 406, L55
de Vaucouleurs, G., de Vaucouleurs, A., & Corwin, H. G. 1995, yCat, 7112, 0
de Vaucouleurs, G., de Vaucouleurs, A., Corwin, H. G., Jr., et al. 1991, Third Reference Catalogue of Bright Galaxies. Volume I: Explanations and References. Volume II: Data for Galaxies between 0^h and 12^h. Volume III: Data for Galaxies between 12^h and 24^h (New York: Springer)
Di Matteo, T., Croft, R. A. C., Springel, V., & Hernquist, L. 2003, ApJ, 593, 56
Di Matteo, T., Springel, V., & Hernquist, L. 2005, Natur, 433, 604
Draine, B. T. 2011, Physics of the Interstellar and Intergalactic Medium (Princeton, NJ: Princeton Univ. Press)
Dressler, A., & Sandage, A. 1983, ApJ, 265, 664
Fabello, S., Kauffmann, G., Catinella, B., et al. 2011, MNRAS, 416, 1739
Fabian, A. C. 1999, MNRAS, 308, L39
Ferrarese, L. 2002, ApJ, 578, 90
Ferrarese, L., & Merritt, D. 2000, ApJL, 539, L9
Fisher, D. 1997, AJ, 113, 950
Franx, M., & de Zeeuw, T. 1992, ApJL, 392, L47
Gebhardt, K., Lauer, T. R., Kormendy, J., et al. 2001, AJ, 122, 2469
Gebhardt, K., Richstone, D., Tremaine, S., et al. 2003, ApJ, 583, 92
Greene, J. E., Peng, C. Y., Kim, M., et al. 2010, ApJ, 721, 26
Greene, J. E., Seth, A., den Brok, M., et al. 2013, ApJ, 771, 121
Guhathakurta, P., van Gorkom, J. H., Kotanyi, C. G., & Balkowski, C. 1988, AJ, 96, 851
Gültekin, K., Richstone, D. O., Gebhardt, K., et al. 2009, ApJ, 698, 198
Gültekin, K., Tremaine, S., Loeb, A., & Richstone, D. O. 2011, ApJ, 738, 17
Halliday, C., Davies, R. L., Kuntschner, H., et al. 2001, MNRAS, 326, 473
Häring, N., & Rix, H.-W. 2004, ApJL, 604, L89
Hirschmann, M., Khochfar, S., Burkert, A., et al. 2010, MNRAS, 407, 1016
Ho, L. C. 2007, ApJ, 668, 94
Ho, L. C., Darling, J., & Greene, J. E. 2008, ApJ, 681, 128
Hopkins, P. F., Hernquist, L., Cox, T. J., et al. 2006, ApJS, 163, 1
Jahnke, K., & Macciò, A. V. 2011, ApJ, 734, 92
Jones, K. L., Koribalski, B. S., Elmouttie, M., & Haynes, R. F. 1999, MNRAS, 302, 649
Kent, S. M. 1990, AJ, 100, 377
Knapp, G. R., van Driel, W., & van Woerden, H. 1985, A&A, 142, 1
Kormendy, J., & Bender, R. 2011, Natur, 469, 377
Kormendy, J., Drory, N., Bender, R., & Cornell, M. E. 2010, ApJ, 723, 54
Kormendy, J., & Ho, L. C. 2013, ARA&A, 51, 511
Krajnović, D., Cappellari, M., de Zeeuw, P. T., & Copin, Y. 2006, MNRAS, 366, 787
Kronawitter, A., Saglia, R. P., Gerhard, O., & Bender, R. 2000, A&AS, 144, 53
Kuo, C. Y., Braatz, J. A., Condon, J. J., et al. 2011, ApJ, 727, 20
Kuo, C.-Y., Lim, J., Tang, Y.-W., & Ho, P. T. P. 2008, ApJ, 679, 1047
Lindblad, P. A. B., Kristen, H., Joersaeter, S., & Hoegbom, J. 1997, A&A, 317, 36
Lodato, G., & Bertin, G. 2003, A&A, 398, 517
Marconi, A., & Hunt, L. K. 2003, ApJL, 589, L21
McConnell, N. J., & Ma, C.-P. 2013, ApJ, 764, 184
Miralda-Escudé, J., & Kollmeier, J. A. 2005, ApJ, 619, 30
Mundell, C. G., Pedlar, A., Axon, D. J., Meaburn, J., & Unger, S. W. 1995, MNRAS, 277, 641
Murphy, J. D., Gebhardt, K., & Adams, J. J. 2011, ApJ, 729, 129
Murray, N., Quataert, E., & Thompson, T. A. 2005, ApJ, 618, 569
Navarro, J. F., Frenk, C. S., & White, S. D. M. 1996, ApJ, 462, 563
Neumayer, N., & Walcher, C. J. 2012, AdAst, 2012, 15
Noordermeer, E., van der Hulst, J. M., Sancisi, R., Swaters, R. S., & van Albada, T. S. 2007, MNRAS, 376, 1513
Novak, G. S., Faber, S. M., & Dekel, A. 2006, ApJ, 637, 96
Ostriker, J. P., Choi, E., Ciotti, L., Novak, G. S., & Proga, D. 2010, ApJ, 722, 642
Paturel, G., Theureau, G., Bottinelli, L., et al. 2003, A&A, 412, 57
Pellegrini, S., Held, E. V., & Ciotti, L. 1997, MNRAS, 288, 1
Peng, C. Y. 2007, ApJ, 671, 1098
Pizzella, A., Corsini, E. M., Dalla Bontà, E., et al. 2005, ApJ, 631, 785
Reid, M. J., Braatz, J. A., Condon, J. J., et al. 2009, ApJ, 695, 287
Reid, M. J., Braatz, J. A., Condon, J. J., et al. 2013, ApJ, 767, 154
Roberts, M. S. 1978, AJ, 83, 1026
Roberts, M. S., & Haynes, M. P. 1994, ARA&A, 32, 115
Robertson, B., Hernquist, L., Cox, T. J., et al. 2006, ApJ, 641, 90
Schiminovich, D., van Gorkom, J. H., van der Hulst, J. M., & Kasow, S. 1994, ApJL, 423, L101
Scorza, C., & Bender, R. 1995, A&A, 293, 20
Shostak, G. S. 1987, A&A, 175, 4
Silk, J., & Rees, M. J. 1998, A&A, 331, L1
Sofue, Y., Tutui, Y., Honma, M., & Tomita, A. 1997, AJ, 114, 2428
Tremaine, S., Gebhardt, K., Bender, R., et al. 2002, ApJ, 574, 740
Valluri, M., Ferrarese, L., Merritt, D., & Joseph, C. L. 2005, ApJ, 628, 137
van der Marel, R. P., & Franx, M. 1993, ApJ, 407, 525
Volonteri, M., & Natarajan, P. 2009, MNRAS, 400, 1911
Volonteri, M., Natarajan, P., & Gültekin, K. 2011, ApJ, 737, 50
Wechsler, R. H., Bullock, J. S., Primack, J. R., Kravtsov, A. V., & Dekel, A. 2002, ApJ, 568, 52
Young, L. M., & Lo, K. Y. 1997, ApJ, 476, 127